Multimodal identification of rare potent effector CD8 T cells in solid tumors

Arja Ray[1,2], Molly Bassette[1,2], Kenneth H. Hu[1,2,#], Lomax F. Pass[1,2], Bushra Samad[2,3], Alexis Combes[1,2,3,5], Vrinda Johri[2,3], Brittany Davidson[2,3], Grace Hernandez[4], Itzia Zaleta-Linares[1,2], Matthew F. Krummel[1,2*]

Affiliations:
[1]Department of Pathology, [2]ImmunoX Initiative, [3]UCSF CoLabs, [4]Department of Anatomy, [5]Department of Medicine, University of California, San Francisco, CA 94143, USA. [#] Current Address: Department of Immunology, The University of Texas MD Anderson Cancer Center and James P Allison Institute

***Corresponding Author:**
Matthew F. Krummel, Ph.D.
513 Parnassus Avenue, HSW 512
San Francisco, CA 94143-0511
matthew.krummel@ucsf.edu
Tel: (415) 514-3130
Fax: (415) 514-3165

Abstract: Antitumor immunity is driven by CD8 T cells, yet we lack signatures for the exceptional effectors in tumors, amongst the vast majority of CD8 T cells undergoing exhaustion. By leveraging the measurement of a canonical T cell activation protein (CD69) together with its RNA (*Cd69*), we found a larger classifier for TCR stimulation-driven effector states *in vitro* and *in vivo*. This revealed exceptional 'star' effectors—highly functional cells distinguished amidst progenitor and terminally exhausted cells. Although rare in growing mouse and human tumors, they are prominent in mice during T cell-mediated tumor clearance, where they engage with tumor antigen and are superior in tumor cell killing. Employing multimodal CITE-Seq allowed de novo identification of similar rare effectors amidst T cell populations in human cancer. The identification of rare and exceptional immune states provides rational avenues for enhancement of antitumor immunity.

One sentence summary: Parsing T cell activation states using a novel reporter mouse reveals the functional identity of potent anti-tumor CD8 T cells

Main Text:

Within broadly immunosuppressive tumor microenvironments (TME), pockets of rare reactive immunity have been discovered, such as those containing conventional type 1 dendritic cells (cDC1s) that support T cells through antigen presentation (*1*). T cells, which integrate their encounters with antigens over their lifetime (*2-4*), require potent antigen stimulation for anti-tumor function. Yet chronic stimulation by persistent antigen in the TME also drives precursor TCF7^{hi} CD8 T cells to dysfunctional or exhausted states (*5*) and cells with phenotypes defined as resident memory (T_{RM}) also show strong evidence of exhaustion(*6*). Although this path to T cell exhaustion is increasingly well understood including developmental stages (*7, 8*), molecular markers (*9-11*), transcriptional, epigenetic (*10-13*) and microenvironmental drivers (*14, 15*) , an intermediate and reactive T cell effector population that emerges from these precursors is not well-defined.

***A novel genetic tool to report T cell stimulation history in vivo*:** While the cell surface expression of a protein like CD69 is often linked to successful T cell stimulation and T cell retention (*16*), our analysis of a series of datasets showed that a history of repeated stimulation is associated with decreasing transcription of the *Cd69* gene. For example, *Cd69* mRNA itself is higher in naïve vs. effector and progenitor vs. terminally exhausted CD8 T cells **(Fig. S1A-C)**, and in conventional T cells in tumor-adjacent normal areas versus those within paired human colorectal cancers (CRC) (**Fig. S1D**). Further mining of related data reveals that the transcription factors regulating *Cd69* transcription were also differentially and systematically lower in exhausted vs. naïve CD8 T cells (**Fig. S1E**). In contrast, CD69 protein expression, driven by TCR stimulation or other stimuli such as interferons (*17*), is often uncoupled from transcriptional activity at this locus by strong 3' UTR-mediated post-transcriptional regulation (*18*). We thus reasoned that tracking *Cd69* RNA alongside its protein may together provide a useful means to differentiate the historical and current effector state of T cells.

To make this tractable, we generated mice in which DNA encoding the teal fluorescent protein (TFP) was inserted at the 5' end of the *Cd69* locus to record its transcriptional activity (hereby referred to as the *Cd69*-TFP reporter) **(Fig. 1A)**. In concert with antibody staining for surface CD69 protein, we thus had a non-invasive way to study, sort and challenge cells with different combinations of RNA and protein expression. In unchallenged *Cd69*-TFP mice, the majority (~80% "Q1", **Fig. 1B**) of CD8 T cells in lymph nodes were TFP^{hi} without expressing surface CD69. Another small population of cells expressed CD69 protein on their cell surface alongside TFP (~5%, "Q2") and a moderate population (~15% "Q3") was low for both TFP and CD69 (**Fig. 1B**). We validated that TFP accurately reflected *Cd69* RNA expression at steady state (**Fig. S2A-B**) and found that the reporter faithfully tracked with well-established CD69 protein upregulation during the early and intermediate stages of thymic positive selection (*19*) as well as during the first 6-18h of stimulation of isolated peripheral T cells with anti-CD3/CD28 beads (**Fig. S3A, B**).

When viewed across differentiation states, we found that TFP expression varied with extent and quality of historical stimulation; $CD44^{hi}CD62L^{lo}$ Effector CD8 T cells expressed levels lower than $CD44^{lo}CD62L^{hi}$ Naïve cells as we had observed in historical datasets and $CD44^{lo}CD62L^{hi}$ central memory T cells (Memory) demonstrated higher levels than either. (**Fig. 1C).** These differences in TFP expression were stable when cells were purified and rested in IL-7 overnight (**Fig. 1D**). Predictably, following short (3h) stimulation with anti-CD3/anti-CD28 beads, TFP^{hi} Memory and TFP^{lo} Effectors (**Fig. S4A**) both rapidly upregulated surface CD69, even when new transcription was blocked by Actinomycin D, but maintained their pre-existing TFP status (**Fig. 1E**). However, *de novo* surface CD69 expression was markedly lower in TFP^{lo} cells upon stimulation as compared to TFP^{hi} (**Fig. 1E-F, Fig. S4B**), consistent with dependency of protein expression on the level of transcript. Together this indicated faithful reporter activity and also that a combination of *Cd69* RNA reporting (TFP) and CD69 protein exposed a difference (i.e. Q2 vs. Q4) between recently activated cells with different histories of antigen experience.

To directly study how *Cd69*-driven TFP levels were related to activation history, we set up repetitive "chronic" stimulation cultures using purified CD8 T cells from *Cd69*-TFP mice. Cells were subjected to 3 cycles of 48h stimulation with 1:1 anti-CD3/anti-CD28 beads, followed by 72h rest under either hypoxia (1.5% O_2 to mimic the TME) or normoxia, in the presence of low concentrations of IL-2 after the first cycle (**Fig. 1G, Fig. S5A**). CD69 protein expression rose after each stimulation, although significantly less so by the 3rd stimulation, while expression of the activation marker CD44 became more pronounced (**Fig 1G, Fig. S5A**). *Cd69*-driven TFP levels also rose following each stimulation, but progressively rested each time to lower levels, an effect that culminated in about a 50% and 30% reduction under hypoxia and normoxia after 3 cycles, respectively (**Fig 1G-H, Fig. S5A, B**). We validated that both native *Cd69* mRNA (**Fig. 1J, Fig. S5C**) as well as the upstream transcription factor *Jun* (**Fig. 1K**), decreased over the cycles, albeit with faster initial decay than TFP, perhaps reflecting a longer half-life of the fluorescent protein as compared to the transcript that it reports. Repeated stimulation concurrently upregulated exhaustion markers such as PD1, CD38 and Tim-3(*20*) (**Fig. 1L, Fig. S5D, E**). Provision of IL-2 in absence of additional anti-CD3/anti-CD28 stimulation (**Fig. S5F**) demonstrated that differentiation (**Fig. S5G**), decline in TFP expression (**Fig S5H**), and acquisition of exhaustion markers (**Fig. S5I**) were not simply a function of time. While declining levels of resting mRNA did not prevent re-expression of TFP and CD69 upon stimulation, it significantly lowered the magnitude of the peaks from Cycle 1 to Cycle 3 (**Fig. 1M, Fig. S5J**), consistent with previous data (**Fig. S4B**). Thus in the Protein:RNA (CD69:TFP) space, trajectories of cell state are not retraced during subsequent activation events—rather, TFP levels decrease with repeated stimulation (**Fig. 1N**)."Q2" cells in this reporter system emerge as ones that are recently activated, yet have not been subject to chronic and exhaustive stimulation.

Delineation of chronic vs. potent activation states in tumors: To translate these observations into the context of tumors, we adoptively transferred *Cd69*-TFP reporter positive ovalbumin-reactive CD8 T cells from CD45.1; OT-I; mice into WT mice bearing B78chOVA (OVA and mCherry expressed in B78 (*14*)) tumors (**Fig. 2A**). Recovered cells were largely in Q1 and Q3 on when they can be first detected at day 4, and by day 6, we found them predominantly in the "Q2" (~60%) $TFP^{hi}CD69^{+}$ state. By day 14, however, they were primarily $TFP^{lo}CD69^{-}$ (Q3) and $TFP^{lo}CD69^{+}$ (Q4) (**Fig. 2B, D).** In contrast, the distribution of adopted cells was more consistent in the draining lymph node (dLN) across time: approximately 60% in Q1 and 15-30% in Q2. (**Fig. 2C, D**). Similar trends were observed in a spontaneous breast carcinoma tumor model (PyMTchOVA)(*21*) (**Fig. S6A, B**).

Even at day 14, Q2 cells expressed less terminal exhaustion markers as compared to those in the TFP^{lo} Q4 in both B78chOVA (**Fig. 2E)** and PyMTchOVA tumors **(Fig. S6C**) and Q4 cells largely became prevalent in tumors approximately 10 days post-adoption (**Fig. 2B-D, Fig. S6A, B**). The decline in the Q2 proportion of OT-Is from d6 to d18 was also accompanied by a decrease in progenitor (Ly108) and increase in terminal exhaustion markers (**Fig. S6D**).

Because ongoing recruitment of T cells from the dLN is difficult to control and may obscure interpretation of these adoptive transfer experiments, we complemented these results by developing a variant of a long-term tumor slice overlay protocol(*22*) where all T cells encounter the tumor microenvironment at once and no new emigrants arrive (**Fig. 2F**). The progression of phenotypes through CD69:TFP quadrants (**Fig. 2G, Fig. S7A)** and the increasing over-representation of cells with an exhausted phenotype in Q4 (**Fig. S7B-D**) recapitulated what we had seen in vivo, suggesting that this is not a result of variations in the lymph-node emigrating pool. Slices also allowed easy analysis of robust proliferation in the slice-infiltrating OT-I T cells over time using violet proliferation dye (VPD) (**Fig. S7E**) which accompanied the general decrease in TFP expression with each division (**Fig. S7F**) and was exemplified at day 3 **(Fig. S7G**). VPD

dilution showed that Q4 cells had typically undergone more division (**Fig. S7H**) as they acquired higher levels of exhaustion (**Fig. 2H**) as compared to Q2 cells, further differentiating these states. This progression is consistent with previous studies of the relationship between chronic tumor residence, proliferation(*23, 24*) and exhaustion, while also again differentiating the population in Q2.

Finally, to determine how this progression is related to antigen detection and the microenvironment in which that antigen is detected, we isolated CD8 T cells with a non-tumoral specificity (LCMV-specific P14; *Cd69*TFP) and compared their state both within a tumor (that does not express their antigen) and within a vaccination site, to that of the OT-Is (**Fig 2I**). P14; *Cd69*TFP cells co-injected with CD45.1; OT-I; *Cd69*TFP T cells into B78chOVA tumor-bearing mice, that also received a priming gp33-41 peptide vaccination distal to the tumor (**Fig. 2I**), were found to express higher TFP levels in the tumor than OT-Is (**Fig. 2J, K**). In contrast to the Q4-rich OT-I T cells in the tumor, P14 T cells at the contralateral vaccination site remained substantially TFP^{hi} with a 4x increase in the frequency of cells Q2 (**Fig. 2J, K**). Hence, exposure to the TME alone did not lead to loss of a Q2 state, and presentation of antigen at a vaccine site stimulated cells in such a way as to maintain that Q2 state.

Marking the highest-quality intratumoral effectors: We next sought to both understand whether Q2 cells were typically better effectors and use transcriptomic analysis to find signatures that tracked best with Q2 cells. We thus isolated OTI; *Cd69* TFP T cells from d12 B78chOVA tumors, sorted and barcoded each population separately for CD69:TFP quadrant and performed single cell RNA Sequencing (scSeq) (**Fig. 3A**). Analysis of this data via Louvain clustering and UMAP projection allowed us to immediately map Q2 in the context of previously defined post-exhaustion T cell states (T_{EX}) (*8*), and other previously named intratumoral states that were based on RNA alone (**Fig. 3B, Fig. S8A**). Our data recapitulated those computationally derived predicted

differentiation trajectories (**Fig. S8B, C**; See Methods) and the expected progression towards terminal exhaustion through the quadrants Q1-Q4 (**Fig. S9**)). Unbiased computational RNA-based clustering alone, however, did not capture a single subset with a superior cytotoxic score (*Prf1, Klrd1, Gzmc, Tnfrsf9, Ifng*), which was variably distributed across multiple subsets, although these are indeed more frequent within with exceptional levels in populations that have previously been named $Tex^{E.Eff}$, Tex^{int} and especially Tex^{KLREff} (**Fig 3C**).

When we overlayed barcodes representing Q2 sorted cells onto this UMAP, we found that these spanned several clusters, and as expected with dominance in those Tex^{Eff} ($Tex^{E.Eff}$, Tex^{KLREff}) populations as well as a subregion of the Tex^{Prog} (**Fig. 3D, Fig. S10A, B**). Further and consistent with our previous observations, parsing these effectors by *Cd69*:TFP quadrant demonstrated the Q2 subset to be low and Q4 to be highest in a signature (*Pdcd1, Cd38, Cd39, Entpd1, Tox*) of exhaustion (**Fig. 3E**). Using this, we sought to use Q2 as an anchor, to characterize the transcriptional signature of the strongest effectors with robust cytotoxicity and limited exhaustion. We did so first by illuminating the intersection of Tex^{Eff} and Q2, identifying a population that perhaps due to its sparsity and subtlety, doesn't otherwise appear as a distinct computational cluster. Performing DGE analysis of Q2 vs. Q4 within that T_{EX}^{Eff}, we found a signature comprising among others the granzyme *Gzmc,* a tetraspannin previously implicated in lymphocyte activation (*25, 26*) *Cd81* and a collection of other genes that are consistent with a unique propensity to interact with other cells such as *Xcl1 (*putatively would attract cDC1*)* and *Ccr7.* Perhaps unsurprisingly for a population that may have unique stimulatory signals, we also found enrichment election of a subset of proliferation-associated genes.(**Fig. 3F**).

The resulting signature, which we term 'star' effectors or T^*_{EFF} for simplicity, highlights a portion of Tex^{Prog} as well as a subset of cells buried within $Tex^{E.Eff}$ and $Tex^{KLR\ Eff}$ on a uMAP projection. (**Fig 3G**). These overlap only partially with cells that express the highest levels of *Tcf7* and are nearly exclusive from those that are highest in markers of exhaustion (**Fig. 3G, Fig. S11A**). The

distribution of this signature also tracks with genes associated with cytotoxicity (e.g. *Ifng*, which notably is not part of the signature), and significantly with *Cd81,* which in contrast is a component of the signature(**Fig. 3G**). Cd81 is a surface protein, making it useful for sorting but turns out to vary in its fidelity for reporting star effector phenotypes across various TME. For example, in the B78chOVA tumors, Q2 was reliably associated with ~3x increases in the mean level of CD81 surface protein expression (**Fig. 3H**), where in other models such as PyMTchOVA showed that this marker can also be found in cells that have not upregulated CD69 protein **(**i.e. Q1, **Fig. S11C)**. Such variability limits absolute use of CD81 as a definitive marker across every tumor and site, and the use of this single marker in the PyMT model may be further limited since $CD81^+$ T^*_{EFF}s were even rarer within these tumors (**Fig. S11B, D**).

Nonetheless, in the B78 tumor model, armed with a refined definition of T^*_{EFF} that could be non-invasively assessed through the combination of the Q2 reporter marking together with CD81 antibody staining, we sought to assess how effector function parsed with this population. For this we sorted OT-I T cells by the CD69:TFP quadrants with CD81 stain from tumors at d12 and assayed for cytokine and granzyme expression following restimulation with PMA/Ionomycin for 3h (**Fig. 3I-L**). Amongst the four quadrants, Q2 cells displayed the maximum functional capacity, both in terms of GzmB expression (**Fig. 3I, K**) and bifunctionality, as measured by TNF-α : IFN-γ double positivity (**Fig. 3J**, **L**). Strikingly, when we selected for CD81+ cells from within the Q2 compartment, i.e., a tighter gate for T^*_{EFF} (**Fig. S11E**), this further enriched for effector function, these cells having 2-10x higher expression of both %$GzmB^+$ and % TNF-α^+-IFN-γ^+ compared to other populations (**Fig. 3I-L**). This data supports that sorting for the T^*_{EFF} signature enriches for high-quality effectors.

Prominence of functional effector pool during anti-tumor response: MC38chOVA tumors are actively controlled in response to the injection of antigen-specific OT-I T cells (**Fig. 4A, Fig. S12A**), whereas B78ChOVA are not. We found that *Cd69*-TFP;OT-I T cells in regressing

MC38chOVA tumors, retain their predominantly Q2 ($CD69^{+}TFP^{+}$) phenotype even at d12 post adoptive transfer, in contrast to those in the growing B78chOVA tumors(**Fig. 4B-C, Fig. S12B**), while the TFP^{hi} proportions in the corresponding dLNs was similar in both (MC38chOVA :**Fig. S12C,** B78chOVA : **Fig. 2C, D**). By two-photon microscopy TFP^{hi} cells could be identified by post-imaging analysis of the appropriate channel intensity over non-TFP controls (**Fig. S12D**). Such analysis showed enhanced cell arrest of the TFP^{hi} within MC38chOVA tumor slices harboring adopted OT-Is, with lower overall motility (**Fig. 4D**), speed (**Fig. S12E**), and persistence of motion (**Fig. S12F)**. In both mouse (*24*) and human(*22*) tumors, these traits are associated with lower T cell exhaustion. Q2 OT-I cells sorted from MC38chOVA tumors also showed the highest killing capacity when exposed to MC38chOVA cells in vitro (**Fig. 4E**). In MC38 as in the B78 model, CD81 was enriched specifically in Q2 cells among intratumoral OT-Is (**Fig. S12G**). Using that surface marking, we found that CD81 was markedly more abundant in the ongoing antigen-specific anti-tumor response in MC38 tumors (**Fig. S12H**), as opposed to non-responsive B78chOVA and PyMTchOVA tumors (**Fig. S11B, D**). Moreover, Q2 and especially CD81+ T^{*}_{EFF}s also enriched for a recently-defined, non-canonical and durable CD39+Ly108+ effector population modestly in B78chOVA and robustly in MC38chOVA tumors. (*27*) (**Fig. S12I**).

De novo identification of star effectors by CITE-Seq in human patients: We next sought to independently identify similar CD8 activation states in human tumors (**Fig. S13A),** now using multimodal CITE-Seq on Head and Neck Squamous Cell Carcinoma (HNSC) tumor biopsies post CD45-enrichment (**Fig. 5A**). We focused first on pooled samples with a large number (~5000) of CD8 T cells, where simultaneous readouts of CD69 mRNA and surface protein allowed CD8 T cells to be gated into 4 quadrants (akin to reporter mice), with notable dominance in Q4 and Q2 (**Fig. S13A, B**). Again, presumably due to their rarity and the unbiased nature of combined protein-RNA driven weighted nearest neighbor determination, we did not isolate all Q2 cells into a single

cluster. In contrast and akin to mouse studies, Q2 highlighted a subset of cells predominantly concentrated within an effector (Eff-1) subset with some also in the Eff-2, Eff-Exh and naive clusters (**Fig. 5B, C, Fig. S13C, D**).

DGE analysis of this small subset of Q2 cells within the Eff-1 cluster (<5% of the total CD8s) revealed a signature comprising of genes associated with activation-related transcription (*CD69,* and also upstream *JUN, FOS, ZFP36, KLF6*) where the former were notably those we initially associated as being downregulated following repeated stimulation. The human-derived signature also included chemokines (*CCL3, CCL4,* both high in the $Tex^{KLR.Eff}$ in mice, **Fig. S8A**, *CCL4L2, XCL2,* closely related to XCL1 found in the mouse signature), as well as effector function (*IFNG, DUSP1,2, NFKBIA, TNFSF9,* etc.), mRNA abundance (*SERTAD1, BTG2*) and proliferation (**Fig. 5D**). In addition to these genes, the analysis also defined surface protein markers differentially upregulated in these T^*_{EFF}s including CCR5 and KLRG1 (**Fig. 5D, Fig. S13E**). Interestingly, the downregulated protein set not only included exhaustion markers CD38, CD39, 2B4, but also CD103 and CD69. Indeed, T_{RM}s as defined simply by $CD69^+CD103^+$ exist both in Q2 and Q4 and their relation to exhaustion markers may be context-dependent(*6*) (**Fig. S13E**). Consistent with evolutionary divergence of immune systems(*28*), we found that RNA signatures were not identical and yet across 10 indications of human cancer (*29*), T cell-specific expression of the human T^*_{EFF} RNA gene signature correlated highly with that of the expression of human homologs of the RNA signature derived from our mouse tumor scSeq in Fig. 3 (**Fig. 5E)**. Further, when this T^*_{EFF} RNA gene signature was overlaid back onto the UMAP, it again highlighted a region intermediate to and distinct from cells having highest expression of naïve and exhaustion markers (**Fig. 5F**). When applied to other HNSC samples (sample 2 and 3), this RNA T^*_{EFF} signature continued to be highest in cells defined by Q2 and distinct from naïve (variably highest in Q1 and Q3) and exhaustion (predictably highest in Q4) markers alike (**Fig. 5G**). Analysis of CD8 T cells in a second and independent pan-cancer T cell atlas(*30*) again revealed localization of T^*_{EFF} RNA-

signature^{hi} cells in the intervening phenotypic space between naïve and exhausted cells (**Fig. 5H, Fig. S14A**). Notably, in this second and larger dataset, the authors had suggested multiple T cell subsets associated with enhanced function such as KLR-expressing NK-like CD8 T cells, ZNF683+CXCR6+ T_{RM} (*31*) and IL7R+ memory T cells (*32*) and these were enriched for T^*_{EFF} RNA-signature, while exhausted and naïve subsets were not (**Fig. S14B**). Such pan-cancer delineation of potent effectors would likely be refined with generation of more datasets with dual protein and RNA expression to define these populations in distinct settings.

In summary, we have defined a multimodal approach to find potently activated CD8 T cells, hidden within the largely exhausted pool in tumors. The systematic use of *Cd69* transcription, along with its surface protein expression may be imminently applicable in other important contexts including vaccination, resident memory formation and autoimmunity, to directly identify and study potent activation states of lymphocytes in situ.

Here we applied this strategy to isolate and validate that this subpopulation of effector CD8 T cells was functionally superior and otherwise not well illuminated by unbiased RNA-based cell clustering within the well-defined exhaustion paradigm. As future studies seek to better understand and manipulate the T^*_{EFF} cells, it is interesting to speculate that chemokines like XCL1/XCL2 would allow T^*_{EFF}s to attract the superior antigen presenting XCR1+ DCs to interact and drive a reactive archetype. These cells may indeed be generated by potent stimulation driven by cDC1s (*33*). While exploration of favorable cDC1 niches and networks continue to drive the field, the identification of functional T^*_{EFF}s now opens up the possibility to focus on directly detecting, studying and ultimately enhancing potent effectors in tumors, as an optimizing strategy to drive better patient outcomes.

References and Notes:

1. M. L. Broz *et al.*, Dissecting the Tumor Myeloid Compartment Reveals Rare Activating Antigen-Presenting Cells Critical for T Cell Immunity. *Cancer Cell* **26**, 938 (2014).
2. D. Masopust, S. J. Ha, V. Vezys, R. Ahmed, Stimulation history dictates memory CD8 T cell phenotype: implications for prime-boost vaccination. *J Immunol* **177**, 831-839 (2006).
3. B. B. Au-Yeung *et al.*, A sharp T-cell antigen receptor signaling threshold for T-cell proliferation. *Proc Natl Acad Sci U S A* **111**, E3679-3688 (2014).
4. J. N. Mandl, J. P. Monteiro, N. Vrisekoop, R. N. Germain, T cell-positive selection uses self-ligand binding strength to optimize repertoire recognition of foreign antigens. *Immunity* **38**, 263-274 (2013).
5. A. Schietinger *et al.*, Tumor-Specific T Cell Dysfunction Is a Dynamic Antigen-Driven Differentiation Program Initiated Early during Tumorigenesis. *Immunity* **45**, 389-401 (2016).
6. M. JJ *et al.*, Heterogenous Populations of Tissue-Resident CD8+ T Cells Are Generated in Response to Infection and Malignancy. *Immunity* **52**, (2020).
7. J. C. Beltra *et al.*, Developmental Relationships of Four Exhausted CD8+ T Cell Subsets Reveals Underlying Transcriptional and Epigenetic Landscape Control Mechanisms. *Immunity* **52**, 825-841.e828 (2020).
8. B. Daniel *et al.*, Divergent clonal differentiation trajectories of T cell exhaustion. (2021).
9. E. J. Wherry *et al.*, Molecular signature of CD8+ T cell exhaustion during chronic viral infection. *Immunity* **27**, 670-684 (2007).
10. O. Khan *et al.*, TOX transcriptionally and epigenetically programs CD8 + T cell exhaustion. *Nature* **571**, 211-218 (2019).
11. M. Philip *et al.*, Chromatin states define tumour-specific T cell dysfunction and reprogramming. *Nature* **545**, 452-456 (2017).
12. Z. Chen *et al.*, TCF-1-Centered Transcriptional Network Drives an Effector versus Exhausted CD8 T Cell-Fate Decision. *Immunity* **51**, 840-855.e845 (2019).
13. A. C. Scott *et al.*, TOX is a critical regulator of tumour-specific T cell differentiation. *Nature* **571**, 270-274 (2019).
14. K. Kersten *et al.*, Spatiotemporal co-dependency between macrophages and exhausted CD8+ T cells in cancer. *Cancer Cell* **40**, 624-638.e629 (2022).
15. B. L. Horton *et al.*, Lack of CD8 + T cell effector differentiation during priming mediates checkpoint blockade resistance in non-small cell lung cancer. *Sci Immunol* **6**, eabi8800 (2021).
16. W. DA *et al.*, The Functional Requirement for CD69 in Establishment of Resident Memory CD8+ T Cells Varies with Tissue Location. *Journal of immunology* **203**, (2019).
17. J. F. Ashouri, A. Weiss, Endogenous Nur77 Is a Specific Indicator of Antigen Receptor Signaling in Human T and B Cells. *J Immunol* **198**, 657-668 (2017).
18. A. G. Santis, M. López-Cabrera, F. Sánchez-Madrid, N. Proudfoot, Expression of the early lymphocyte activation antigen CD69, a C-type lectin, is regulated by mRNA degradation associated with AU-rich sequence motifs. *Eur J Immunol* **25**, 2142-2146 (1995).
19. T. M. McCaughtry, M. S. Wilken, K. A. Hogquist, Thymic emigration revisited. *J Exp Med* **204**, 2513-2520 (2007).

20. N. E. Scharping *et al.*, Mitochondrial stress induced by continuous stimulation under hypoxia rapidly drives T cell exhaustion. *Nature Immunology* **22**, 205-215 (2021).
21. J. J. Engelhardt *et al.*, Marginating dendritic cells of the tumor microenvironment cross-present tumor antigens and stably engage tumor-specific T cells. *Cancer Cell* **21**, 402-417 (2012).
22. R. You *et al.*, Active surveillance characterizes human intratumoral T cell exhaustion. *J Clin Invest* **131**, (2021).
23. H. Li *et al.*, Dysfunctional CD8 T Cells Form a Proliferative, Dynamically Regulated Compartment within Human Melanoma. *Cell* **176**, 775-789 e718 (2019).
24. B. Boldajipour, A. Nelson, M. F. Krummel, Tumor-infiltrating lymphocytes are dynamically desensitized to antigen but are maintained by homeostatic cytokine. *JCI insight* **1**, e89289 (2016).
25. Y. Sagi, A. Landrigan, R. Levy, S. Levy, Complementary costimulation of human T-cell subpopulations by cluster of differentiation 28 (CD28) and CD81. *Proc Natl Acad Sci U S A* **109**, 1613-1618 (2012).
26. K. J. Susa, T. C. Seegar, S. C. Blacklow, A. C. Kruse, A dynamic interaction between CD19 and the tetraspanin CD81 controls B cell co-receptor trafficking. *Elife* **9**, (2020).
27. J.-C. Beltra *et al.*, Enhanced STAT5a activation rewires exhausted CD8 T cells during chronic stimulation to acquire a hybrid durable effector like state. (2022).
28. T. Shay *et al.*, Conservation and divergence in the transcriptional programs of the human and mouse immune systems. *Proc Natl Acad Sci U S A* **110**, 2946-2951 (2013).
29. A. J. Combes *et al.*, Discovering dominant tumor immune archetypes in a pan-cancer census. *Cell* **185**, 184-203.e119 (2022).
30. L. Zheng *et al.*, Pan-cancer single-cell landscape of tumor-infiltrating T cells. *Science* **374**, abe6474 (2021).
31. M. Di Pilato *et al.*, CXCR6 positions cytotoxic T cells to receive critical survival signals in the tumor microenvironment. *Cell* **184**, 4512-4530 e4522 (2021).
32. G. Micevic *et al.*, IL-7R licenses a population of epigenetically poised memory CD8(+) T cells with superior antitumor efficacy that are critical for melanoma memory. *Proc Natl Acad Sci U S A* **120**, e2304319120 (2023).
33. J. CS *et al.*, An intra-tumoral niche maintains and differentiates stem-like CD8 T cells. *Nature* **576**, (2019).
34. K. C. Barry *et al.*, A natural killer-dendritic cell axis defines checkpoint therapy-responsive tumor microenvironments. *Nat Med* **24**, 1178-1191 (2018).
35. M. K. Ruhland *et al.*, Visualizing Synaptic Transfer of Tumor Antigens among Dendritic Cells. *Cancer Cell* **37**, 786-799.e785 (2020).
36. Y. S. Tan, Y. L. Lei, Isolation of Tumor-Infiltrating Lymphocytes by Ficoll-Paque Density Gradient Centrifugation. *Methods Mol Biol* **1960**, 93-99 (2019).
37. C. S. McGinnis *et al.*, MULTI-seq: sample multiplexing for single-cell RNA sequencing using lipid-tagged indices. *Nat Methods* **16**, 619-626 (2019).
38. G. Oliveira *et al.*, Phenotype, specificity and avidity of antitumour CD8+ T cells in melanoma. *Nature* **596**, 119-125 (2021).

39. S. J. Carmona, I. Siddiqui, M. Bilous, W. Held, D. Gfeller, Deciphering the transcriptomic landscape of tumor-infiltrating CD8 lymphocytes in B16 melanoma tumors with single-cell RNA-Seq. *Oncoimmunology* **9**, 1737369 (2020).
40. E. Kim *et al.*, Inositol polyphosphate multikinase is a coactivator for serum response factor-dependent induction of immediate early genes. *Proc Natl Acad Sci U S A* **110**, 19938-19943 (2013).
41. A. Litvinchuk *et al.*, Complement C3aR Inactivation Attenuates Tau Pathology and Reverses an Immune Network Deregulated in Tauopathy Models and Alzheimer's Disease. *Neuron* **100**, 1337-1353.e1335 (2018).
42. A. S. Stephens, S. R. Stephens, N. A. Morrison, Internal control genes for quantitative RT-PCR expression analysis in mouse osteoblasts, osteoclasts and macrophages. *BMC Res Notes* **4**, 410 (2011).
43. A. Dobin *et al.*, STAR: ultrafast universal RNA-seq aligner. *Bioinformatics* **29**, 15-21 (2013).
44. B. Li, C. N. Dewey, RSEM: accurate transcript quantification from RNA-Seq data with or without a reference genome. *BMC Bioinformatics* **12**, 323 (2011).
45. H. G. Othmer, S. R. Dunbar, W. Alt, Models of dispersal in biological systems. *J Math Biol* **26**, 263-298 (1988).
46. R. B. Dickinson, R. T. Tranquillo, Optimal estimation of cell movement indices from the statistical analysis of cell tracking data. AIChE Journal Volume 39, Issue 12. *AIChE Journal*. 1993.

Acknowledgments:

Funding:

National Institutes of Health Grants: NIH R01CA197363 and NIH R37AI052116

AR was supported by a Cancer Research Institute Postdoctoral Fellowship (CRI2940)

KHH was supported by an American Cancer Society and Jean Perkins Foundation Postdoctoral Fellowship

GH was supported by the National Science Foundation Graduate Research Fellowship Program (NSF2034836)

IZL was supported by Emerson Collective Health Research Scholars Program

We thank Dr. Emily Flynn, UCSF for guidance with the CITE-Seq analysis. We thank Dr. Kelly Kersten, UCSF, Dr. Mike Kuhns, University of Arizona and Dr. Miguel Reina-Campos, University of California San Diego, for critical reading of the manuscript. We also thank Dr. Reina-Campos

for sharing data from Zheng et.al in an analysis-ready format. We thank members of the Krummel lab for their inputs to the manuscript.

Author Contributions:

Conceptualization: AR, MFK

Experimentation: AR, MB, GH, LFP, IZL

Mouse scSeq: KHH, AR

Human tumor data analysis: AR, AJC, BS

Human tumor data collection: VD, BD, AJC

Funding acquisition: MFK, AR, KHH

Writing: AR, MFK

Supervision: MFK

Competing Interests:

The authors declare no competing interests

Data materials availability:

Relevant data will be made publicly available before publication in its final form. Meanwhile, data will be available upon reasonable request, please contact the authors directly.

List of Supplementary Materials:

Materials and Methods

Fig. S1-S14

Figures and Figure Legends:

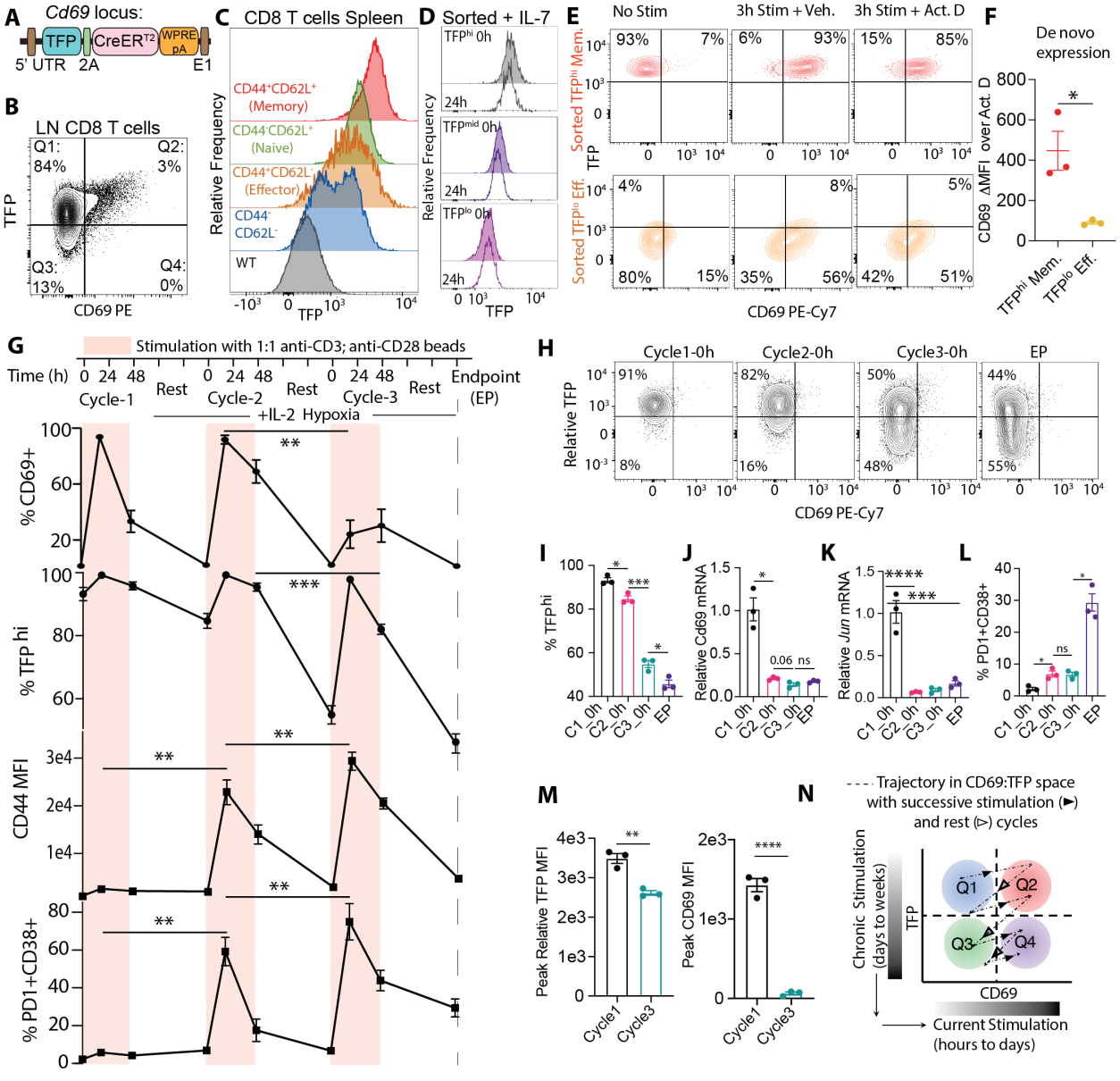

Fig.1: Cd69-TFP reporter reads out history of T cell stimulation

(A) Design of the TFP-2A-CreER^{T2}-WPRE-pA reporter knocked into the 5' UTR of the *Cd69* locus; **(B)** TFP vs. CD69 in homeostatic lymph node (LN) CD8 T cells with percentage of cells in each quadrant; **(C)** representative histograms of TFP expression in splenic CD8 T cells of different phenotypes (as indicated in the figure panel) from an unchallenged Cd69-TFP reporter mouse; **(D)** characteristic histograms of TFP expression from flow cytometry data from sorted TFP^{hi} (top 20%), TFP^{mid} (middle 30%) and TFP^{lo} (bottom 20%) of splenic and lymph node-derived CD8 T cells at 0h and 24h post sort, resting in IL-7; **(E)** flow cytometry

plots of TFP vs. CD69 in sorted TFP^{lo} Effector and TFP^{hi} Memory homeostatic CD8 T cells without stimulation (No Stim), 3h αCD3+αCD28 stimulation + DMSO (3h Stim + Vehicle) or 5μg/mL Actinomycin D (3h Stim + Act.D) and **(F)** relative change in CD69 MFI between the Vehicle and Act D treated conditions (de novo expression) in the two sorted groups, from data in S4B; **(G)** %CD69+, %TFP^{hi}, CD44 MFI, %PD1^{+}CD38^{+} of freshly isolated CD8 T cells through successive cycles of 48h stimulation and 72h resting in hypoxia + IL-2; **(H)** representative flow cytometry plots showing TFP vs. CD69, **(I)** %TFP^{hi}, **(J)** *Cd69* mRNA and **(K)** *Jun* mRNA by qPCR, **(L)** %PD1^{+}CD38^{+} at the beginning of cycles 1, 2, 3 and endpoint (EP); **(M)** Peak Relative TFP and CD69 MFI between Cycle 1 and Cycle 3; **(N)** schematic showing the trajectory of CD8 T cells within the TFP:CD69 states (quadrants) with successive stimulation and rest, providing a reading of historic of stimulation. (Plots show mean +/- SEM; TFP negative gates derived from corresponding WT controls; statistical testing by ANOVA and post-hoc Holm-Šídák test; n=3 biological replicates representative of at least 2 independent experiments).

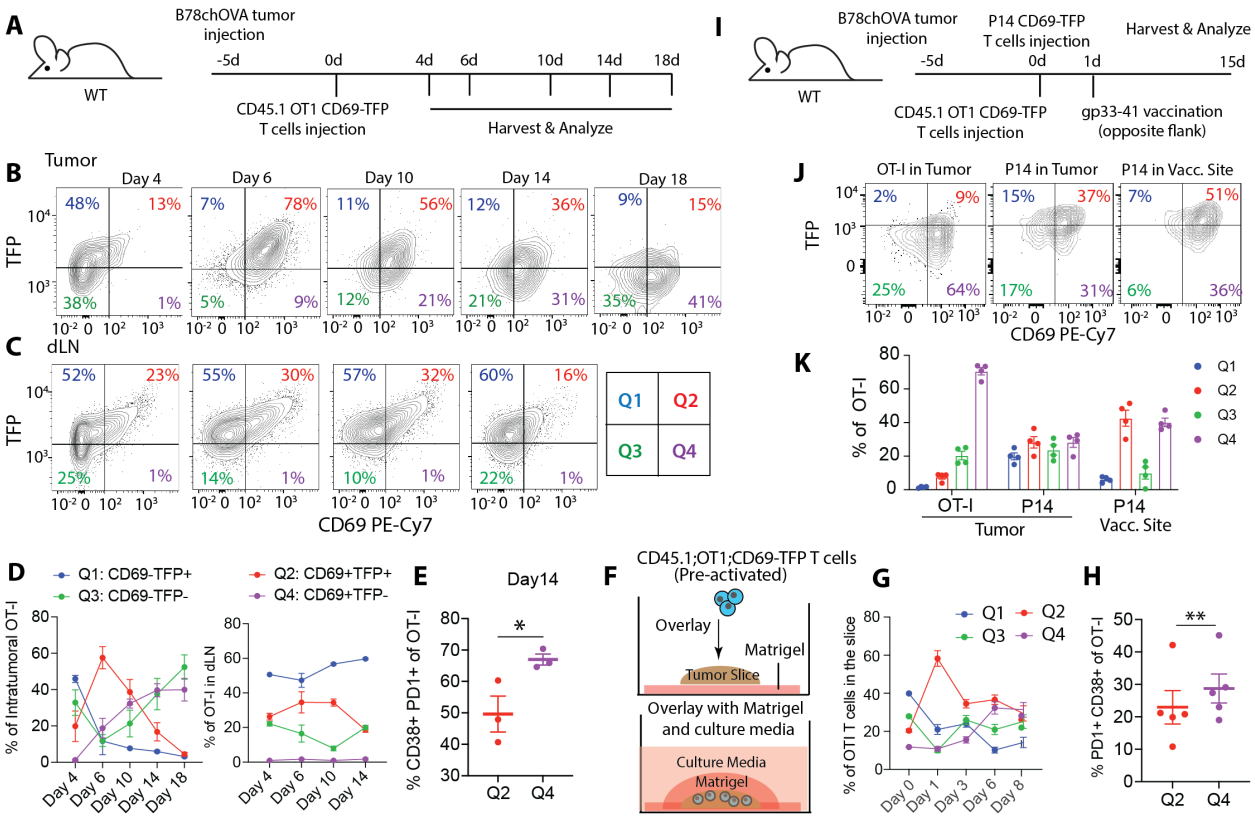

Fig. 2: Delineation of potent versus dysfunctional CD8 T cell activation states in tumors

(A) Experimental schematic to track antigen-specific T cells in B78chOVA tumors over time; Flow cytometry plots showing TFP vs. CD69 of adoptively transferred OT-I T cells from **(B)** B78chOVA tumors and **(C)** corresponding tumor-draining lymph nodes (dLN) over time with the **(D)** CD69:TFP quadrant (Q1-Q4) distribution for the same; **(E)** %CD38+PD1+ terminally exhausted cells among activated d14 intratumoral OT-Is belonging to TFP^{hi} Q2 and TFP^{lo} Q4; **(F)** Schematic representation of long-term tumor slice culture setup; pre-activated: 48h stimulation with αCD3+αCD28 followed by 48h rest in IL-2; **(G)** CD69:TFP quadrant distribution and **(H)** $\%PD1^{+}CD38^{+}$ of slice-infiltrating OT-I T cells at d8; **(I)** Experimental schematic of tumor injection and contralateral vaccination with orthogonal antigen specificities; **(J)** Flow cytometry plots showing TFP vs. CD69 profiles of OT-I, P14 T cells in the OVA+ tumor and P14 T cells at the gp33-41 vaccination (vacc.) site; **(K)** CD69:TFP quadrant distribution of the same. (Representative data from 2-3 independent experiments, 3-4 mice or 5-6 slices/timepoint/experiment, pre-slice-overlay samples in duplicate, plots show mean +/- SEM, *p <0.05, **p<0.01 by paired t-tests in E and H).

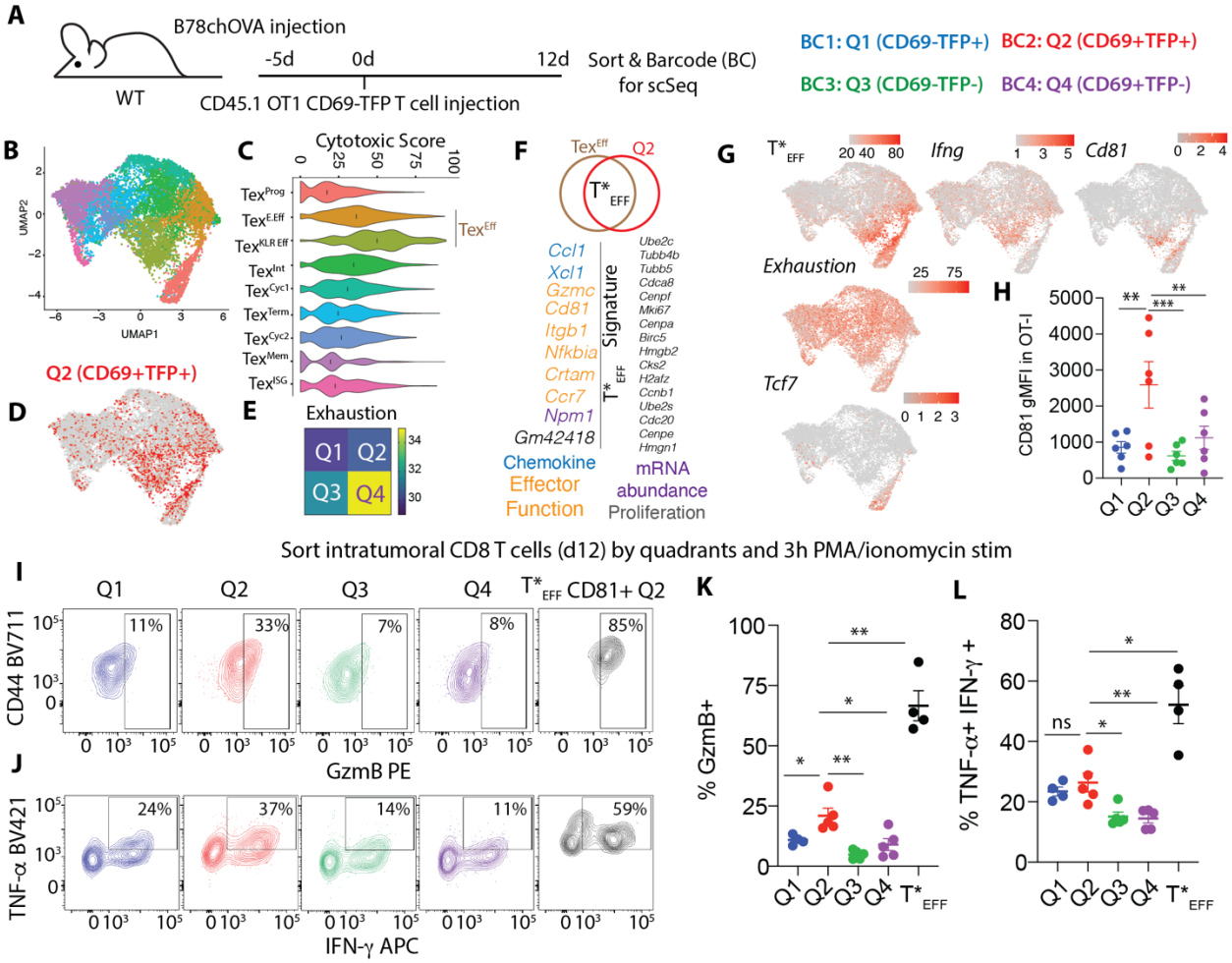

Fig. 3: Single-cell mapping of activation states reveals functionally endowed intratumoral effectors (A) Experimental schematic for single cell transcriptomic profiling of intratumoral OT-I T cells sorted by CD69:TFP quadrants; **(B)** UMAP representation of the scSeq data color-coded by computationally-derived clusters; **(C)** Cytotoxic scoring of the T cell subsets (black lines =median); **(D)** overlay of Q2 ($CD69^{+}TFP^{+}$) in the UMAP space; **(E)** Heatmap exhaustion score of combined T_{EX}^{Eff} subsets by quadrants; **(F)** Differentially upregulated genes in in Q2 vs. Q4 within the T_{EX}^{Eff} cells to define T^{*}_{EFF} signature (color-coded text indicates predicted function of similarly colored genes); **(G)** Overlay of T^{*}_{EFF} signature score, *Ifng, Cd81,* Exhaustion Score, and *Tcf7* in the UMAP space; **(H)** CD81 expression in d14 intratumoral OT-I T cells grouped by quadrants; Intracellular expression of **(I)** GzmB, **(J)** TNF-α and IFN-γ in intratumoral OT-I T cells sorted by quadrants and restimulated, with a sub-gating of $CD81^{+}$ cells from Q2, with **(K and L)** corresponding quantification. pooled data from 2 independent experiments with 2-3 biological replicates (sorted cells from 2-3 tumors each)/experiment (K, L). Plots show mean +/- SEM; null hypothesis testing by paired RM ANOVA with post-hoc paired t-tests.

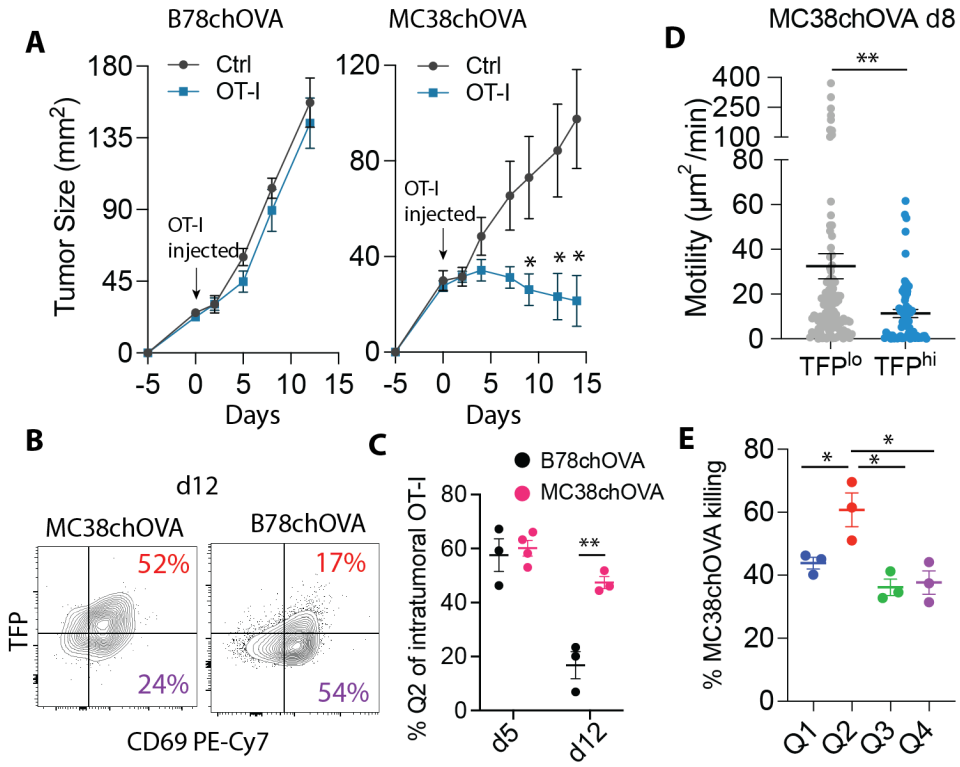

Fig. 4: Prominence of potent CD8 effectors in favorable anti-tumor response

(A) Contrasting growth curves of B78chOVA and MC38chOVA with and without OT-I transfer 5 days post tumor injection, as indicated by the color-coded arrows (n=5-6/group); **(B)** Typical flow cytometry plot of TFP vs. CD69 of intratumoral OT-Is d12 post adoptive transfer with **(C)** quantification of the percentage of Q2 cells at d5 and d12 in the two tumor models; **(D)** Motility of TFP^{hi} vs. TFP^{lo} intratumoral OT-Is d8 post adoptive transfer within live MC38chOVA tumor slices; **(E)** in vitro killing of MC38chOVA cells by OT-I T cells sorted by CD69:TFP quadrants from d8 MC38chOVA tumors; Bar plots show mean +/- SEM; n > 100 cells per group pooled from at least 2 slices each from different tumors (D); null hypothesis testing by unpaired t test (C), Mann-Whitney U test (D), ANOVA with post-hoc Holm-Šídák test (E).

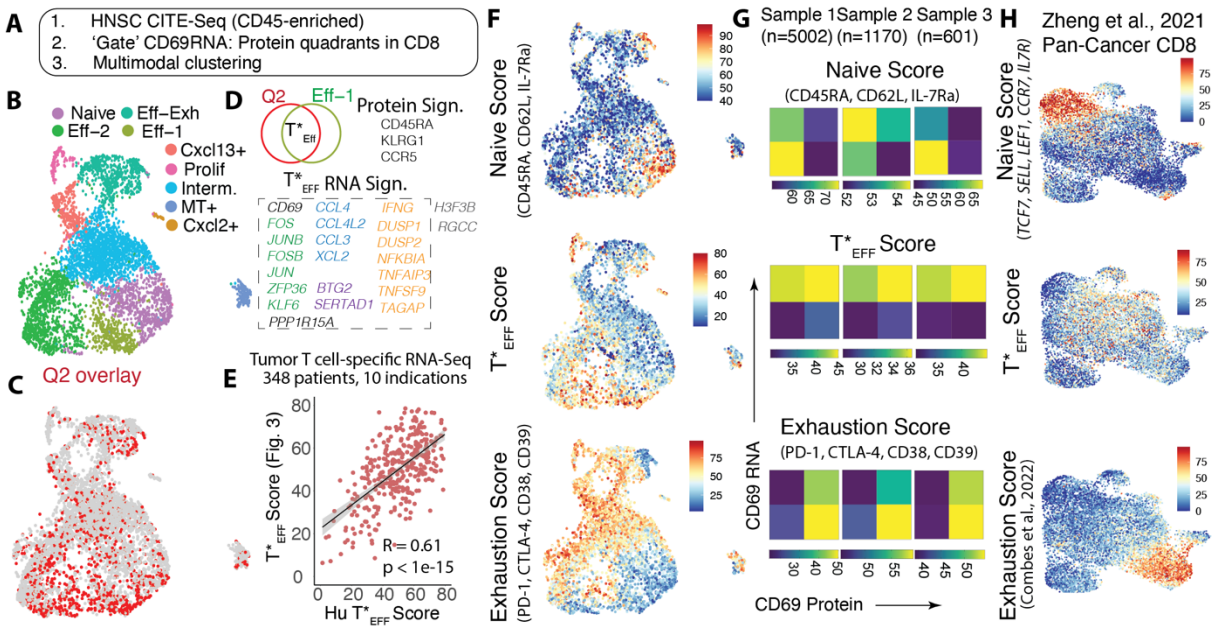

Fig. 5: De novo identification of potent effectors in human cancer by CITE-Seq

(A) Schematic description of human HNSC tumor CITE-Seq analysis; (B) UMAP showing weighted nearest neighbor (WNN) determined clusters by multimodal RNA and Protein analysis; (C) overlay of Q2 cells (determined by gating on CD69 Protein and RNA – Fig.S13B) on the UMAP; (D) Differentially upregulated genes and proteins in the T^*_{EFF} (Q2 ∩ Eff-1) cells vs. all others CD8 T cells, genes color-coded by functional category, box indicates genes used for the T^*_{EFF} gene signature; **(E)** Correlation between this human T^*_{EFF} gene signature and that from human orthologs of the gene signature in Fig. 3F **(F)** Naïve, T^*_{EFF} and Exhaustion scores overlayed on the WNN UMAP, and **(G)** Heatmap representation of median levels of the same scores in CD8 T cells from 3 different patient samples split into CD69 protein: CD69 mRNA quadrants; (n: # of CD8 T cells in each sample); **(H)** Naïve, T^*_{EFF} and Exhaustion scores overlaid onto the UMAP of combined CD8 T cells from a previously published pan-cancer atlas (*30*).

Supplementary Materials for

Multimodal identification of rare potent effector CD8 T cells in solid tumors

Arja Ray[1,2], Molly Bassette[1,2], Kenneth H. Hu[1,2,#], Lomax F. Pass[1,2], Bushra Samad[2,3], Alexis Combes[1,2,3,5], Vrinda Johri[2,3], Brittany Davidson[2,3], Grace Hernandez[4], Itzia Zaleta-Linares[1,2], Matthew F. Krummel[1,2*]

Affiliations:

[1]Department of Pathology, [2]ImmunoX Initiative, [3]UCSF CoLabs, [4]Department of Anatomy, [5]Department of Medicine, University of California, San Francisco, CA 94143, USA. [#] Current Address: Department of Immunology, The University of Texas MD Anderson Cancer Center and James P Allison Institute

***Corresponding Author:**
Matthew F. Krummel, Ph.D.
513 Parnassus Avenue, HSW 512
San Francisco, CA 94143-0511
matthew.krummel@ucsf.edu
Tel: (415) 514-3130
Fax: (415) 514-3165

Materials and Methods

Mice: All mice were treated in accordance with the regulatory standards of the National Institutes of Health and American Association of Laboratory Animal Care and were approved by the UCSF Institution of Animal Care and Use Committee. Cd69-TFP-CreER^{T2} (denoted as Cd69-TFP) mice in the C57BL6/J background were custom-generated from Biocytogen Inc. and then maintained heterozygous (bred to C57BL6/J wild type mice) at the UCSF Animal Barrier facility under specific pathogen-free conditions. C57BL6/J (wild type; WT), C57BL6/J CD45.1 (B6.SJL-Ptprc^{a} Pepc^{b}/BoyJ), OT-I (C57BL/6-Tg(TcraTcrb)1100Mjb/J) mice were purchased for use from Jackson Laboratories and maintained in the same facility in the C57BL6/J background. For adoptive transfer experiments, CD45.1^{het}; OT-I^{het}; Cd69-TFP^{het} (denoted simply as CD45.1; OT1; Cd69-TFP) mice were used. Mice of either sex ranging in age from 6 to 14 weeks were used for experimentation. For experiments using the transgenic PyMTchOVA strain(*21*), mammary tumor-bearing females in the age range of 15 to 24 weeks were used. Adoptive transfer of T cells in these mice were done when mice developed at least 2 palpable tumors (> 25-30mm^2).

Mouse tumor digestion and flow cytometry: Tumors from mice were processed to generate single cell suspensions as described previously(*34*). Briefly, tumors were isolated and mechanically minced on ice using razor blades, followed by enzymatic digestion with 200 µg/mL DNAse (Sigma-Aldrich), 100U/mL Collagenase I (Worthington Biochemical) and 500U/mL Collagenase IV (Worthington Biochemical) for 30 min at 37°C while shaking. Digestion was quenched by adding excess 1X PBS, filtered through a 100µm mesh, spun down and red blood cells were removed by incubating with RBC lysis buffer (155 mM NH_4Cl, 12 mM $NaHCO_3$, 0.1 mM EDTA) at room temperature for 10 mins. The lysis was quenched with excess 1X PBS, spun down and resuspended in FACS buffer (2mM EDTA + 1% FCS in 1X PBS) to obtain single cell suspensions. Similarly, tumor draining lymph nodes (dLN) were isolated and mashed over 100µm filters in PBS to generate single cell suspensions.

For each sample, 2.5-3 million cells/sample were stained in a total of 50µL of antibody mixture for flow cytometry. Cells were washed with PBS prior to staining with Zombie NIR Fixable live/dead dye (1:500) (Biolegend) for 20 min at 4°C. Cells were washed in FACS buffer followed by surface staining for 30 min at 4°C with directly conjugated antibodies diluted in FACS buffer containing 1:100 anti-CD16/32 (Fc block; BioXCell) to block non-specific binding. Antibody dilutions ranged from 1:100-1:400, optimized separately. After surface staining, cells were washed again with FACS buffer. For intracellular staining, cells were fixed for 20 min at 4°C using the IC Fixation Buffer (BD Biosciences) and washed in permeabilization buffer from the FoxP3 Fix/Perm Kit (BD Biosciences). Antibodies against intracellular targets were diluted in permeabilization buffer containing 1:100 Fc Block and cells were incubated for 30 min at 4°C followed by another wash prior to readout on a BD LSRII or Fortessa Cytometer.

Processing and flow cytometry analysis of other mouse organs: To phenotype T cells under from lymphoid organs homeostasis, spleen and inguinal, mesenteric and brachial lymph nodes were isolated and mashed over 100µm filters washed with 1X PBS to generate single cell suspension of lymphocytes. For splenic suspensions, RBC lysis was performed as described above before staining for flow cytometry.

To profile thymocytes, thymus was isolated, cut into small pieces with a razor blade and minced by using gentleMACS dissociator (Miltenyi Biotec) in RPMI. Next, the mixture was spun down and resuspended in the digestion mixture described above and allowed to digest with shaking at 37°C for 20 mins, following which, the remaining tissue was either minced again using the gentleMACS dissociator and/or directly mashed over a 100µm filter in FACS buffer to generate a single cell suspension, ready to be processed for staining and flow cytometry.

Skin digestion was done as previously described(*35*). Briefly, mice are shaved and depilated prior to removal of dorsal skin. The skin was then rid of fat, minced with scissors and razor blade in the presence of 1 ml of digest media (2 mg/ml collagenase IV (Roche), 1 mg/ml hyaluronidase

(Worthington), 0.1 mg/ml DNase I (Roche) in RPMI-1640 (GIBCO). The minced skin was then moved to a 50 ml conical with 5 ml additional digest solution and incubated at 37°C for 45 min with shaking and intermittent vortexing before being washed and passed through a 70µm strainer prior to staining. TFP high vs. low gates were drawn by using a side-by-side WT control or using endogenous CD8 T cells in the context of adoptive transfer into a tumor-bearing mouse.

Tumor injections and adoptive transfer of CD8 T cells into tumors: The B78chOVA and MC38chOVA cancer cell lines, as previously described(*14, 34*), were generated by incorporating the same mcherry-OVA construct used to establish the PyMTchOVA spontaneous mouse line(*21*). For tumor injections, the corresponding cells were grown to near confluency (cultured in DMEM with 10% FCS (Benchmark) and 1% PSG (Gibco)) and harvested using 0.05% Trypsin-EDTA (Gibco) and washed 3x with PBS (Gibco). The number of cells to be injected per mouse was resuspended in PBS and mixed in a 1:1 ratio with Growth Factor Reduced Matrigel (Corning) to a final volume of 50µL per injection. The mixture was injected subcutaneously into the flanks of anesthetized and shaved mice. Tumors were allowed to grow for 14–21 days unless otherwise noted, before tumors and tumor-draining lymph nodes were harvested for analysis. CD8 T cells were isolated from CD45.1;OT-1;Cd69-TFP mice using the EasySep Negative Selection Kit (Stem Cell Bio), resuspended in 1X PBS at 10X concentration 100µL was injected into each tumor-bearing mice. For B78chOVA and PyMTchOVA tumors, 1 million and for MC38chOVA tumors, 200,000 CD8 T cells were injected retro-orbitally into each mouse either 5d (B78chOVA), 7d (MC38chOVA) post tumor injection or when mice had at least 2 palpable tumors (PyMTchOVA). Tumor measurements were done by measuring the longest dimension (length) and approximately perpendicular dimension (width) using digital calipers, rounded to one decimal place each.

Contralateral tumor injection and vaccination: 5 days post B78chOVA tumor injection, equal numbers (1 million) CD8 T cells from a CD45.1;OT-I;Cd69TFP and P14;Cd69TFP mice were injected retroorbitally into each mice. Next day, gp33-41 subcutaneous peptide (Anaspec)

vaccination was injected contralaterally to the tumor, with 50µg peptide + 50µL Common Freund's Adjuvant (CFA, Sigma) along with 50µL PBS for a total volume of 100µL. The vaccination site was identified by a white, hardened subcutaneous mass and isolated and processed similarly to the tumor for flow cytometry.

In vitro stimulation of naïve CD8 T cells: CD8 T cells were isolated from Cd69-TFP or WT mice as described above and plated in a 96 well round bottom plate (Corning) at 80,000 cells/well in T cell media-RPMI (Gibco) + 10% FCS (Benchmark) + Penicillin/Streptomycin + Glutamine (Gibco). TCR stimulation was induced by adding anti-CD3/CD28 Dynabeads (Applied Biosystems) at the concentration of 2µL per 80,000 cells (1:1 ratio of cells:beads), the plate was briefly spun down to bring cells and beads together before incubation at 37°C for varying lengths of time. 55µM β-mercaptoethanol (BME; Gibco) was added to the T cell media during stimulation. For repeated stimulation assays, 2 wells of each sample at every time point were pooled for mRNA isolation and qRT-PCR, while 2 other wells were used as duplicates for flow cytometry. After each cycle, beads taken off each well and replated for resting in T cell media containing 10 U/mL of Interleukin-2 (IL-2; Peprotech). To restart each stimulation cycle, cells from each biological replicate were pooled, counted and Dynabeads were added at the appropriate concentration for a 1:1 ratio and redistributed into wells for incubation.

Sorting and qPCR, resting or restimulation of homeostatic CD8 T cells: To sort sufficient CD8 T cells from homeostatic lymphoid organs, CD8 T cells were first isolated from spleens and inguinal, brachial, mesenteric lymph nodes Cd69-TFP or WT mice using the EasySep Negative selection kit. These cells were then sorted on TFP^{hi} (top 15%), TFP^{mid} (middle 30%) and TFP^{lo} (bottom 15%) from each mouse separately and rested in T cell media containing 10 U/mL Interleukin-7 in a 96 well round bottom plate and assayed at 0, 24 and 48h. Likewise, for qPCR analysis of populations high, mid and low for TFP, these populations were sorted into cold T cell media, pelleted and subjected to RNA extraction and qPCR with primers for Cd69 and 18s rRNA

as the reference gene. For the sort and restimulation experiment, Memory (CD44+CD62L+) TFP^{hi} cells and Effector (CD44+CD62L-) TFP^{lo} cells were sorted and incubated in T cell media + 55μM BME containing 1:1 anti CD3/CD28 Dynabeads in a 96 well round bottom plate with either 5μg/mL Actinomycin D (Sigma) in DMSO or DMSO alone (vehicle) for 3h, before profiling by flow cytometry. De novo CD69 surface expression was measured by the difference of CD69 MFI between the vehicle and Actinomycin D treated groups.

Restimulation and cytokine production of intratumoral CD8 T cells: OT-I T cells from B78chOVA tumors were sorted on a BD FACSAria Fusion or BD FACSAria2 (BD Biosciences) at d11-d13 post adoptive transfer of CD8 T cells from CD45.1; OT-I; Cd69-TFP mice, as described above. To prepare CD45-enriched fractions(*36*), tumors were digested as described above into single cell suspensions, centrifuged and resuspended in 30mL room temperature (RT) RPMI 1640. Then, 10mL Ficoll-Premium 1.084 (Cytiva) was carefully underlaid and the tubes centrifuged at 1025g for 20 mins at RT without braking. The resulting interface-localized cells were pipetted out, diluted in equal volume RPMI and centrifuged at 650g for 5 mins to collect the cells. This constituted a CD45-enriched fraction which was then processed for staining and FACS. The four CD69:TFP quadrants were sorted from each tumor sample (cells from 2-3 tumor samples were pooled for a single biological replicate) into serum-coated microcentrifuge tubes containing cold T cell media. These were subsequently plated in a 96-well V-bottom plate either in T cell media or T cell media containing PMA (50 ng/mL; Sigma-Aldrich), Ionomycin (500ng/mL; Invitrogen) + Brefeldin A (3μg/mL; Sigma-Aldrich) and BME (Gibco) for 3h, before cells were collected for surface and intracellular staining for cytokines and granzyme B.

Long-term ex vivo tumor slice overlay: Tumor slice overlay cultures were adapted, modified and extended from previous work(*22*). For tumor slice overlay cultures, B78chOVA tumors were injected bilateral subcutaneously into the flank of anesthetized and shaved mice. Tumors were allowed to grow for 11 – 13 days. 96 hours prior to tumor harvest and slicing, CD8 T cells were

677 isolated from CD45.1;OT-1;Cd69-TFP mice, as described above. Isolated CD8 T cells were
678 activated via 1:1 culture with Dynabeads Mouse T-Activator CD3/CD28 (Invitrogen) in T cell
679 media + BME in 96 well U-bottom plates for 48 hours. After activation, T cells were removed from
680 Dynabeads rested in T cell media with supplemented 10 U/mL IL-2 (PeproTech) for 48 hours
681 before use. For gating TFP high vs. low cells, CD8 T cells from CD45.1; OT-I mice were subjected
682 to similar pre-treatment and profiled by flow cytometry side-by-side along with the CD45.1;OT-
683 1;Cd69-TFP CD8 T cells at d0.

684 For slicing, tumors were harvested and stored in cold RPMI until use. Each well of a 24 well plate
685 was pre-filled with cold RPMI and stored on ice. Tumors were embedded in 1.5-2% agarose gel,
686 allowed to solidify, and sliced at a thickness of 350 – 400μm using a Compresstome VF310-0Z
687 Vibrating Microtome (Precisionary). Slices were immediately stored in pre-filled 24 well plate on
688 ice until use.

689 For the slice overlay, each well of a 24 well plate was pre-coated with 30μL of 1 part culture
690 medium:4 parts Matrigel and allowed to solidify at 37˚C. Tumor slices were removed from RPMI
691 and excess agarose was trimmed from slice edges (leaving a thin halo of agarose around slices
692 to use for handling). Slices were spread across solidified Matrigel bed in 24 well plates. Rested T
693 cells were stained with Violet Proliferation Dye 450 (BD Biosciences) diluted 1:1000 in PBS at 10
694 x 10^6 cells/mL for 15 minutes at 37˚C. Cells were washed 2x with PBS and resuspended in T cell
695 culture medium at 150 – 200 x 10^6 cells/mL. 5μL cell suspension (0.5 – 1 x 10^6 cells) was added
696 directly on top of each slice and incubated at 37˚C for 3 hours, with 5μL fresh media added to
697 each slice every 30 minutes to prevent slices from drying out. After incubation, 30μL non-diluted
698 Matrigel was added directly atop each slice and allowed to solidify at 37˚C. 2mL T cell culture
699 medium containing BME was added to each well. 1mL culture medium was removed and replaced
700 with fresh medium every 24 hours throughout the experiment.

Single cell RNA Sequencing and Analysis: Adoptively transferred CD45.1; OT-I; Cd69-TFP CD8 T cells were sorted from B78chOVA tumors d12 post transfer into four populations based on the CD69:TFP quadrants (Q1: TFP+/CD69-, Q2: TFP+/CD69+, Q3: TFP-/CD69-, and Q4: TFP-/CD69+). Sorted cells were separately labeled with lipid and cholesterol-modified oligonucleotides (LMO's) according to McGinnis et. al(*37*). Following 2 washes with PBS + 0.1% BSA, cells were pooled for encapsulation in one lane of a 10X 3' v3 kit with a target cell number of 18,000.

Following construction of the GEX library (according to manufacturer's instructions) and the LMO library(*37*), libraries were pooled at a 10:1 molar ratio for sequencing on the NovaSeq 6000. This resulted in 807M cDNA reads and 163M LMO reads. Transcript and LMO reads were counted using the CellRanger count function against the GRCm38 reference genome to generate feature barcode matrices. These matrices were loaded into Seurat and filtered to remove high mitochondrial % cells (> 15%) and cells with low nGene (< 200 genes). Cells were then demultiplexed using their LMO counts with cells having too few LMO nUMI or ambiguous identity (possible multiplets) filtered out using the demultiplex package(*37*). The resulting object had an average cDNA nUMI per cell of 7662 reads and average nGene per cell of 2115 genes and average LMO nUMI per cell of 1080 reads. The final object underwent scaling and then scoring for cell cycle signatures (S and G2M scores as computed using Seurat's built-in CellCycleScoring function. The object then underwent regression for cell cycle effects (S and G2M score as described in the Seurat vignette) and percent mitochondrial reads before PCA. K-Means clustering and UMAP dimensional reduction was then performed on the first 16 PC's.

Established subpopulations of exhausted T cells were marked by expression of canonical genes such as Stem-like or Progenitor (T_{EX}^{Prog}; *Tcf7, Ccr7, Jun*) (*8, 12*), Early Effector-like ($T_{EX}^{E.Eff}$; *Hsp90aa1, Hsp90ab1, Npm1*) (*38*), Late Effector or KLR-gene-expressing effector-like ($T_{EX}^{KLR.\ Eff}$; *Klrd1, Zeb2*) (*8*), Memory T_{EX}^{Mem}. (*Cxcr3, Ly6c2, Itgb7)* (*39*) and Interferon-Stimulated T_{EX}^{ISG} (*Cxcl10, Isg15, Ifit1*) (**Fig. S8A**). The Intermediate ($T_{EX}^{Int.}$) and Terminal ($T_{EX}^{Term.}$) subsets were

distinguished by exhaustion-related genes *Ctla4, Pdcd1, Tox* and those related to actin organization and TCR signaling such as *Tmsb4x, Coro1a, Actg1, Ccl5 and S100a6(8).* Additionally, two cell cycle gene-dominated clusters termed T_{EX}^{Cyc1} T_{EX}^{Cyc2} were identified (**Fig. 3B, Fig. S8A**).

Cytotoxic and exhaustion scores were generated by calculating the average expression of ensemble gene lists for each of the phenotypes—Exhaustion: *Ctla4, Pdcd1, Cd38, Entpd1, Tox*; Cytotoxic: *Prf1, Gzmc, Tnfrsf9, Ifng, Klrd1*.

qRT-PCR: At designated time points, CD8 T cells were isolated from the 96 well culture plates, or CD8 T cells were sorted into T cell media and centrifuged. The supernatant was aspirated out and the pellets stored at -80˚C until mRNA extraction using the RNEasy Micro Kit (Qiagen). Corresponding cDNA was synthesized from the mRNA samples using the cDNA amplification kit (Applied Biosystems). qPCR using pre-designed *Cd69* and *18s* probes (Invitrogen) with a TaqMan-based assay system (BioRad) or custom-made primers (iDT Technologies) for *Jun* (Fwd: 5′ ACGACCTTCTACGACGATGC 3′, Rev: 5′ CCAGGTTCAAGGTCATGCTC 3′)(*40*) , *Stat5a* (Fwd: 5’ CGCTGGACTCCATGCTTCTC 3’, Rev: 5’ GACGTGGGCTCCTTACACTGA 3’)(*41*) and *18s* (Fwd: 5’ CTTAGAGGGACAAGTGGCG 3’, Rev: 5’ ACGCTGAGCCAGTCAGTGTA 3’)(*42*) using the SsoFast assay system (BioRad) was used to quantify transcripts in a BioRad CFX94 machine.

Human tumor samples: All tumor samples were collected with patient consent after surgical resection under a UCSF IRB approved protocol (UCSF IRB# 20-31740), as described previously(*29*). In brief, freshly resected samples transported in ice-cold DPBS or Leibovitz’s L-15 medium before digestion and processing to generate a single-cell suspension. The following cancer indications were included in the cohort: Bladder cancer (BLAD), colorectal cancer (CRC), glioblastoma multiforme (GBM), gynecological cancers (GYN), hepatocellular cancers (HEP), head and neck cancer (HNSC), kidney cancer (KID), lung cancer (LUNG), melanoma (MEL),

pancreatic ductal adenocarcinoma (PDAC), pancreatic neuroendocrine tumors (PNET), sarcoma (SRC).

Transcriptomic analysis of human tumors: All tumor samples were collected under the UCSF Immunoprofiler project as described(*29*). Briefly, tumor samples were thoroughly minced with surgical scissors and transferred to GentleMACs C Tubes containing 800 U/ml Collagenase IV and 0.1 mg/ml DNase I in L-15/2% FCS per 0.3 g tissue. GentleMACs C Tubes were then installed onto the GentleMACs Octo Dissociator (Miltenyi Biotec) and incubated for 20 min (lymph node) or 35 min (tumor) according to the manufacturer's instructions. Samples were then quenched with 15 mL of sort buffer (PBS/2% FCS/2mM EDTA), filtered through 100µm filters and spun down. Red blood cell lysis was performed with 175 mM ammonium chloride, if needed. Freshly digested tumor samples were sorted by FACS into conventional T cell, Treg, Myeloid, tumor and in some cases, stromal compartments and bulk RNA-seq was performed on sorted cell fractions. mRNA was isolated from sorted fractions and libraries were prepared using Illumina Nextera XT DNA Library Prep kit. The libraries were sequenced using 100bp paired end sequencing on HiSeq4000. The sequencing reads we aligned to the Ensembl GRCh38.85 transcriptome build using STAR(*43*) and gene expression was computed using RSEM(*44*). Sequencing quality was evaluated by in-house the EHK score, where each sample was assigned a score of 0 through 10 based on the number of EHK genes that were expressed above a precalculated minimum threshold. The threshold was learned from our data by examining the expression distributions of EHK genes and validated using the corresponding distributions in TCGA. A score of 10 represented the highest quality data where 10 out of 10 EHK genes are expressed above the minimum threshold. The samples used for survival analysis and other gene expression analyses had an EHK score of greater than 7 to ensure data quality. Ensemble gene signatures scores

were calculated by converting the expression of each gene in the signature to a percentile rank among all genes and then determining the mean rank of all the genes in the signature.

Reanalysis of published datasets: Available, curated RNA-Seq data (*5, 7, 14*) on *Cd69* and upstream transcription factor expression was plotted directly without modification. A curated R object derived from Zheng et al.(*30*) generously shared by Dr. Miguel Reina-Campos, UCSD, was used for analysis in Fig. 5. Ensemble gene signatures were scored as mentioned above and plotted onto pre-existing UMAP dimensional reduction and already annotated cell clusters. While exhaustion and T^*_{EFF} genes were obtained from previously published work (*29*) and this study respectively, *TCF7, SELL, LEF1, CCR7, IL7R* genes were used for the Naïve score.

In vitro Killing Assay: MC38chOVA tumors with adoptively transferred Cd69-TFP-OT-I CD8 T cells in WT B6 mice were harvested at d8 post T cell transfer, digested as mentioned above, and sorted by CD69: TFP quadrants into cold T cell media. Sorted cells were centrifuged, resuspended in fresh, warm T cell media with BME and added onto MC38chOVA cells plated ~24h prior in flat-bottom 96 well plates. To each well containing 5000 MC38chOVA plated 24h prior, 5000 sorted T cells were added. As with the sort and restimulation experiments, each such collection of 5000 cells from a particular quadrant was pooled from 2-3 tumors and treated as a single biological replicate. Each experiment involved 7-8 tumors to obtain at least 3 biological replicates. Technical replicates were included and averaged wherever possible, i.e., at least 10,000 cells were sorted from a given quadrant and biological replicate. Percentage killing was obtained by measuring the fractional loss of live cells at 36h in no T cell vs. T cell added conditions relative to 0h. Live cell numbers from each condition was accurately measured by lightly detaching

cancer cells with trypsin and scoring against CountBright (ThermoFisher) absolute counting beads on a flow cytometer.

CITE-Seq analysis of human tumors: For CITE-Seq, post tumor digestion, cells were incubated with Human TruStain FcX Receptor Blocking Solution to prevent non-specific antibody binding before staining with Zombie Aqua Fixable Viability Dye and anti-human CD45 antibody in PBS/2%FCS/2mM EDTA/0.01% sodium azide and incubated for 25 min on ice in the dark. Live $CD45^+$ and CD45- cells were sorted on a BD FACSAria Fusion. $CD45^+$ and $CD45^-$ cells were pelleted and resuspended at 1x10^3 cells/ml in 0.04%BSA/PBS buffer before mixing in an 8:2 CD45+:CD45- ratio and loaded onto the Chromium Controller (10X Genomics) to generate 5′ v1.1 gel beads-in-emulsions (GEM). Pooled 8:2 CD45+:CD45- cells were resuspended in Cell Staining Buffer (BioLegend) and stained with a pool of 137 TotalSeq-C antibodies (Table) according to the manufacturer's protocol before loading onto the Chromium Controller (10X Genomics) for GEM generation. The cDNA libraries were generated using all or a subset of Chromium Next GEM Single Cell 5′ Library Kit for gene expression (GEX), Chromium Single Cell V(D)J Enrichment kit (10X Genomics) for T cell receptor (TCR), and Chromium Single Cell 5′ Feature Barcode Library kit for antibody derived tag (ADT) according to the manufacturer's instructions. The libraries were subsequently sequenced on a Novaseq S4 sequencer (Illumina) to generate fastqs with the following mean reads per cell: 42,000 (GEX), 34,000 (TCR), and 5,700 (ADT). For multimodal clustering and analysis, CLR normalization followed by weighted nearest neighbor (WNN) clustering was performed using the Seurat package in R. Naïve and Exhaustion scores were generated using the percentile rank method as mentioned above, but with protein (ADT) markers- Naïve : CD62L, CD45RA, IL7RA; Exhaustion: PD-1, CTLA-4, CD38, CD39.

Live 2-photon imaging of tumor slices and image analysis: Live imaging of tumor slices was performed on a custom-made 2-photon microscope as previously described(*1*). Briefly, 1 million CD2dsRed; OT-I; Cd69-TFP or control CD2dsRed; OT-I CD8 T cells were retro-orbitally injected into WT mice bearing MC38chOVA tumors injected 5-7d earlier and harvested 7-10d after T cell injection. Slices for imaging were generated as described above for the ex vivo slice culture assay. Slices were placed in a custom-made perfusion chamber and imaged under oxygenated and temperature-controlled perfusion of RPMI 1640, as described previously(*1*). Dual laser excitations at 825nm and 920nm were used to excite the requisite fluorophores. Image analysis was performed on Imaris (BitPlane) with custom-made plugins developed on Matlab (Mathworks) and Fiji. Surfaces were generated on CD8 T cells and in both CD2dsRed; OT-I and CD2dsRed; OT-I; Cd69-TFP bearing slices and the corresponding levels of the former in the 515-545nm range PMT were used to gate on TFP^{hi} vs. TFP^{lo} OT-Is.

Cell tracking was performed on Imaris and corresponding cell positions imported to Matlab for further analysis to fit the persistent random walk model (PRWM) to the cell trajectories(*45*) using the method of overlapping intervals (*46*). Briefly, the mean squared displacement (MSD) for a cell for given time interval t_i was obtained from the average of all squared displacements x_{ik} such that

$$\bar{x_i} = \frac{1}{n_i}\sum_{k=1}^{n_i} x_{ik} \quad (1)$$

and

$$n_i = N - i + 1 \quad (2)$$

where n_i is the number of overlapping time intervals of duration t_i and N the total number of time intervals for the experiment. Mathematically, the persistent random walk model can be written as

$$MSD(t) = n_d S^2 P[t - P\left(1 - e^{-\frac{t}{P}}\right)] \quad (3)$$

where S is the migration speed and P is the persistence time. The motility coefficient is given as

$$\mu = S^2 P \quad (4)$$

where n_d is the dimensionality of the random walk (in this case n_d=3). We fitted the PRWM in 3D to obtain estimates of speed, persistence time and motility of each cell track by non-linear regression.

Statistical Analysis: Statistical analysis was done in GraphPad Prism or in R. For testing null hypothesis between two groups, either Student's t tests and or the non-parametric Mann-Whitney U tests were used, depending on the number and distribution of data points. Likewise, for testing null hypotheses among 3 or more groups, ANOVA or non-parametric tests were performed, followed by post-hoc Holm-Sidak's test, correcting for multiple comparisons. Unless otherwise mentioned, data are representative of at least 2 independent experiments.

Supplementary Figures:

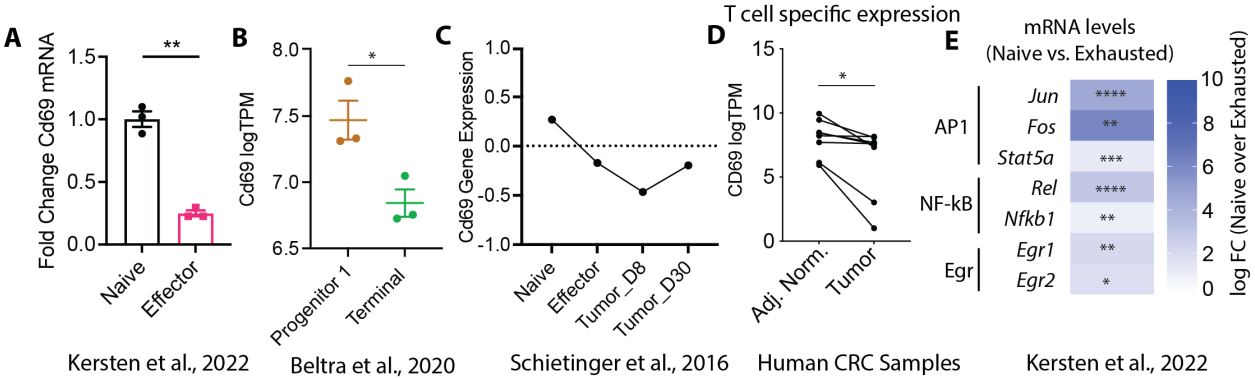

Fig. S1: **Resting Cd69 mRNA decreases with T cell differentiation towards exhaustion.** Cd69 mRNA expression in **(A)** Naïve vs. in vitro generated (stimulation with Dynabeads followed by rest in IL-2 containing media) effector CD8 T cells from published RNASeq data(*14*); **(B)** Progenitor 1 and Terminally exhausted T cell subsets from published data (*7*), **(C)** among Naïve, Effector, D8 tumor and D30 tumor infiltrating T cells from other published data (*5*), **(D)** in conventional T cells sorted from tumor and adjacent normal regions of human colorectal cancer patients; **(E)** depressed mRNA expression of factors associated with the Cd69 transcription in Naïve vs. Exhausted CD8 T cells from previous work (*14*) (symbols indicate FDR adjusted p-values). Plots show mean +/- SEM (A, B) p-values obtained by unpaired (A, B) and paired Student's t test (D).

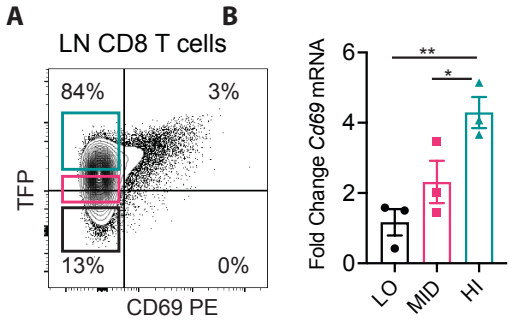

Fig. S2: Cd69-TFP reporter reads out Cd69 transcription. **(A)** TFP vs. CD69 in homeostatic lymph node (LN) CD8 T cells with percentage of cells in each quadrant and **(B)** corresponding *Cd69* mRNA by qPCR from color-coded sorted subpopulations.

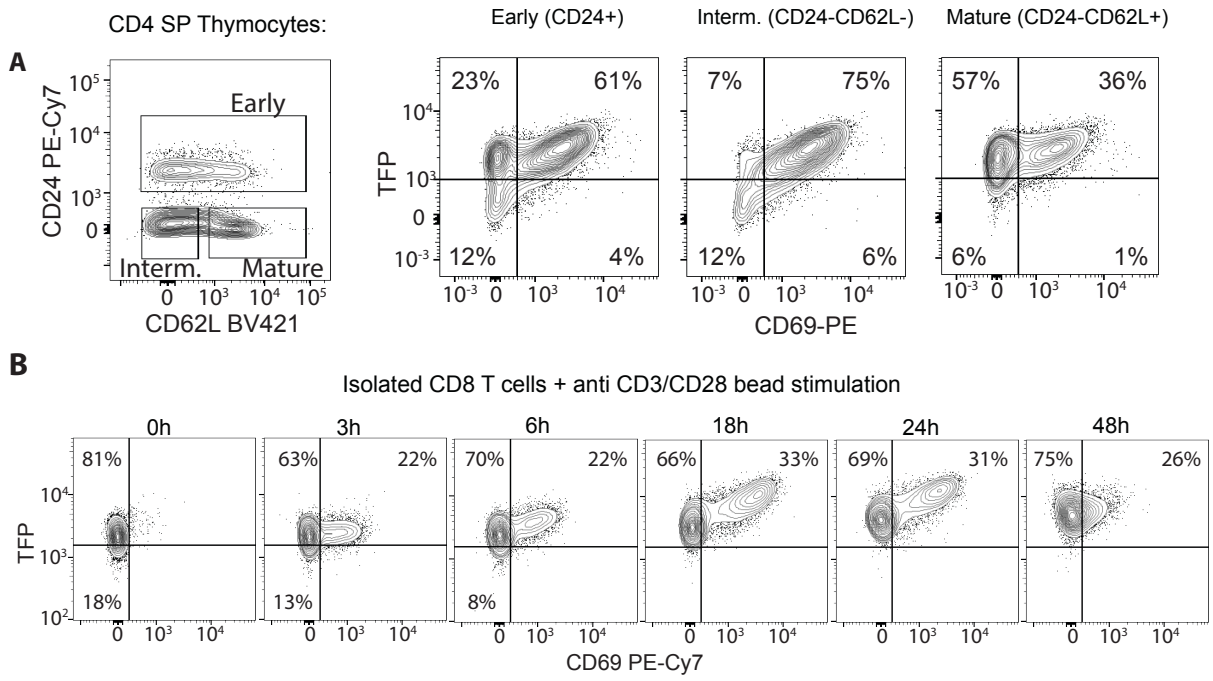

Fig. S3: TFP is upregulated along with CD69 in known contexts of TCR stimulation. (A) Representative flow cytometry plot of CD62L and CD24 expression in CD4+CD8- (CD4 single positive or SP) thymocytes to demarcate early, intermediate (interm.) and mature subsets with corresponding plots of TFP vs. CD69 in these subsets with varying degree of maturity during positive selection; **(B)** Representative flow cytometry plots of TFP vs. CD69 of isolated CD8 T cells from a naïve reporter mouse at different time points post stimulation with αCD3+αCD28 Dynabeads;

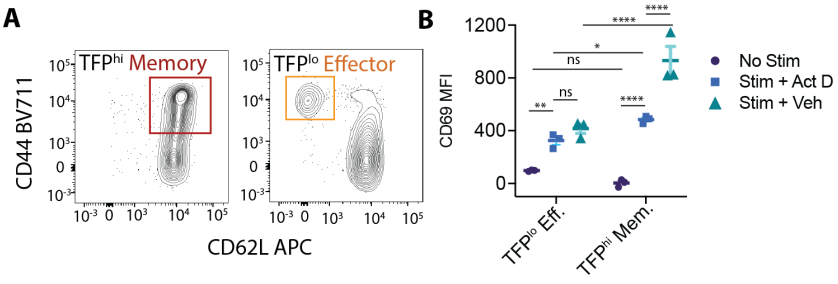

Fig. S4: Sensitivity to current stimulation is dependent on initial TFP level. (A) Typical phenotypic profile shown by flow cytometry plots of CD44 vs. CD62L from TFP^{lo} (bottom 20%) and TFP^{hi} (top 20%) splenic CD8 T cells, sorted TFP^{lo} Effector and TFP^{hi} Memory cells are shown by the corresponding color-coded gates matched with Fig. 1E; **(B)** CD69 MFI of the same sorted cells without stimulation (No Stim), 3h αCD3+αCD28 stimulation + DMSO (3h Stim + Vehicle) or 5μg/mL Actinomycin D (3h Stim + Act.D); (data representative of one out of at least 2 independent

experiments, each with 3 mice, bar graphs show mean +/- SEM, null hypothesis testing by unpaired t test, adjusted for multiple comparisons).

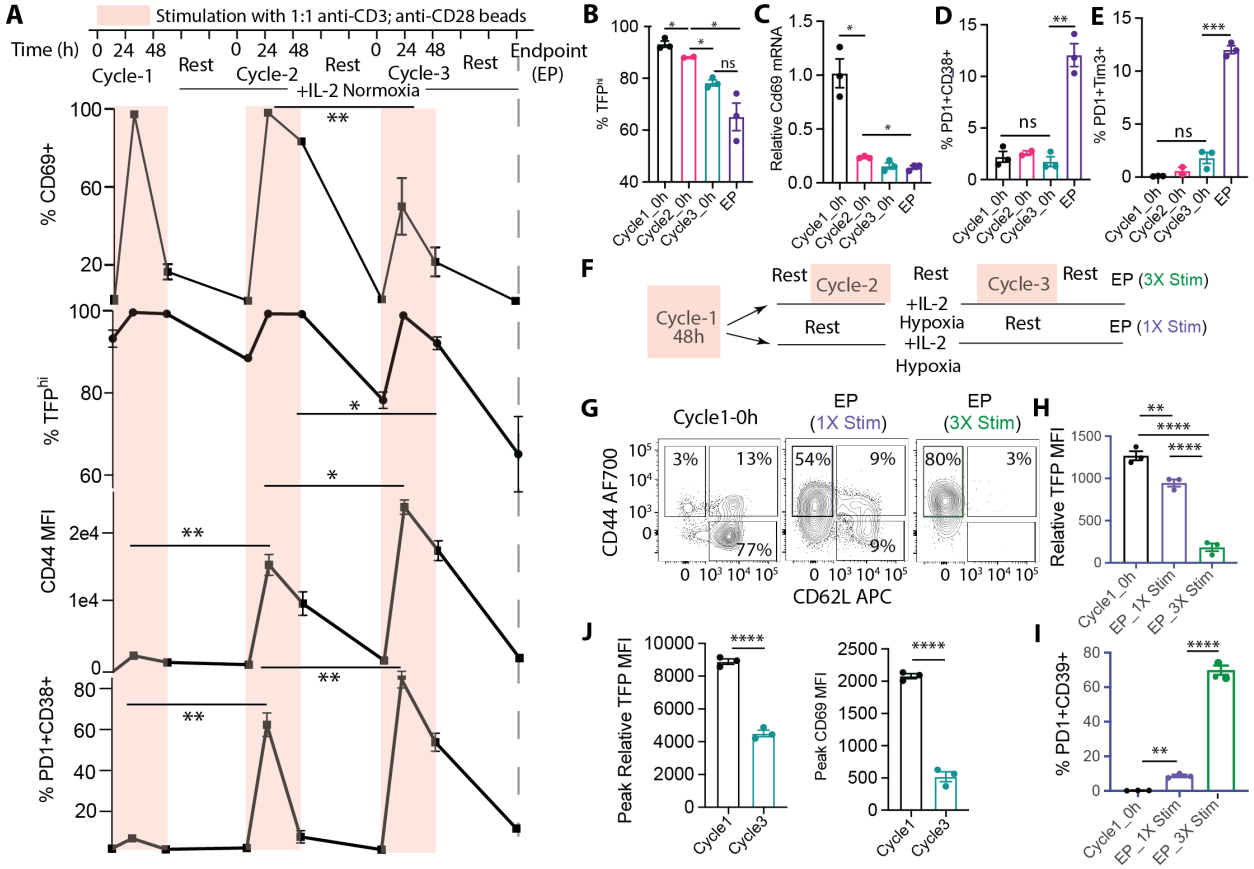

Fig. S5: **Repeated TCR stimulation drives down TFP with acquisition of exhaustion markers** **(A)** %CD69+, %TFP^{hi}, CD44 MFI, %PD1^{+}CD38^{+} of freshly isolated CD8 T cells through successive cycles of 48h stimulation and 72h resting in ambient oxygen (normoxia) + IL-2; **(B)** %TFP^{hi}, **(C)** *Cd69* mRNA by qPCR and **(D)** %PD1^{+}CD38^{+}, **(E)** %PD1^{+}Tim-3^{+} at the beginning of cycles 1, 2, 3 and endpoint (EP); **(F)** experimental schematic showing 1X Stim vs. 3X Stim conditions to parse the role of stimulation vs. IL-2 alone; **(G)** flow cytometry plots showing representative CD44 vs. CD62L profiles of CD8 T cells at the timepoints and conditions indicated; for the same experiment, **(H)** TFP (relative to WT control), **(I)** %PD1^{+}CD39^{+} of CD8 T cells at the starting point (Cycle1_0h) and at endpoint (EP) either with 1X Stim followed by prolonged rest or 3X stim; **(J)** Peak Relative TFP and CD69 MFI between Cycle 1 and Cycle 3 in normoxia; (bar graphs represent mean +/- SEM; null hypothesis testing by ANOVA followed by post-hoc Holm-Šídák test; data representative of 2 independent experiments, each with 3 mice and technical duplicates/biological replicate at every assay point).

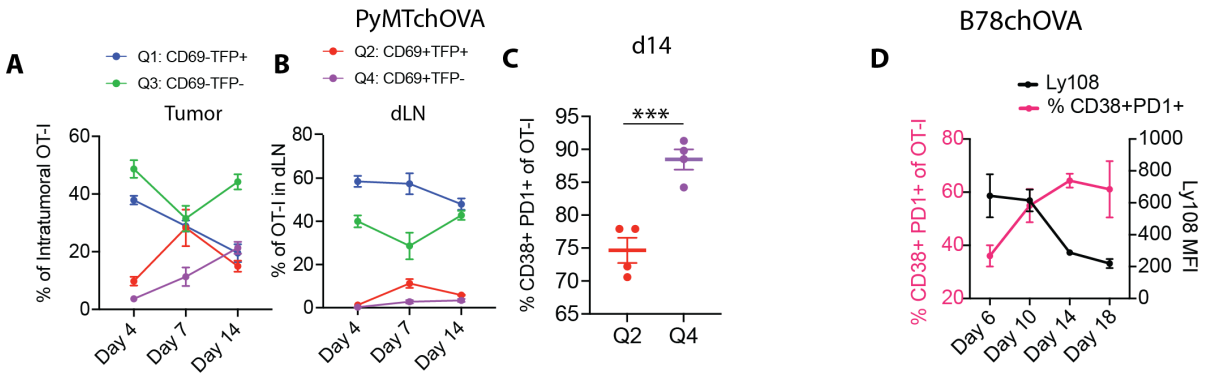

917

Fig. S6: Q4, as opposed to Q2 phenotype dominates terminally exhausted OT-Is in tumors

(A) TFP:CD69 quadrant distribution of OT-I T cells from a PyMTchOVA tumor or its corresponding **(B)** dLN at different time points post injection into tumor-bearing mice; **(C)** %$CD38^{+}PD1^{+}$ terminally exhausted cells among activated d14 intratumoral OT-Is belonging to TFP^{hi} Q2 and TFP^{lo} Q4 from PyMTchOVA tumors; **(D)** %CD38+PD1+ and Ly108 profiles over time (d6-d18) for all intratumoral OT-Is in B78chOVA. Null hypothesis testing by paired t test, bar graphs represent mean +/- SEM; data representative of 2 independent experiments, each with 2-3 mice for PyMTchOVA (each PyMTchOVA mice produced more than one tumor) and >=3 mice for B78chOVA per timepoint.

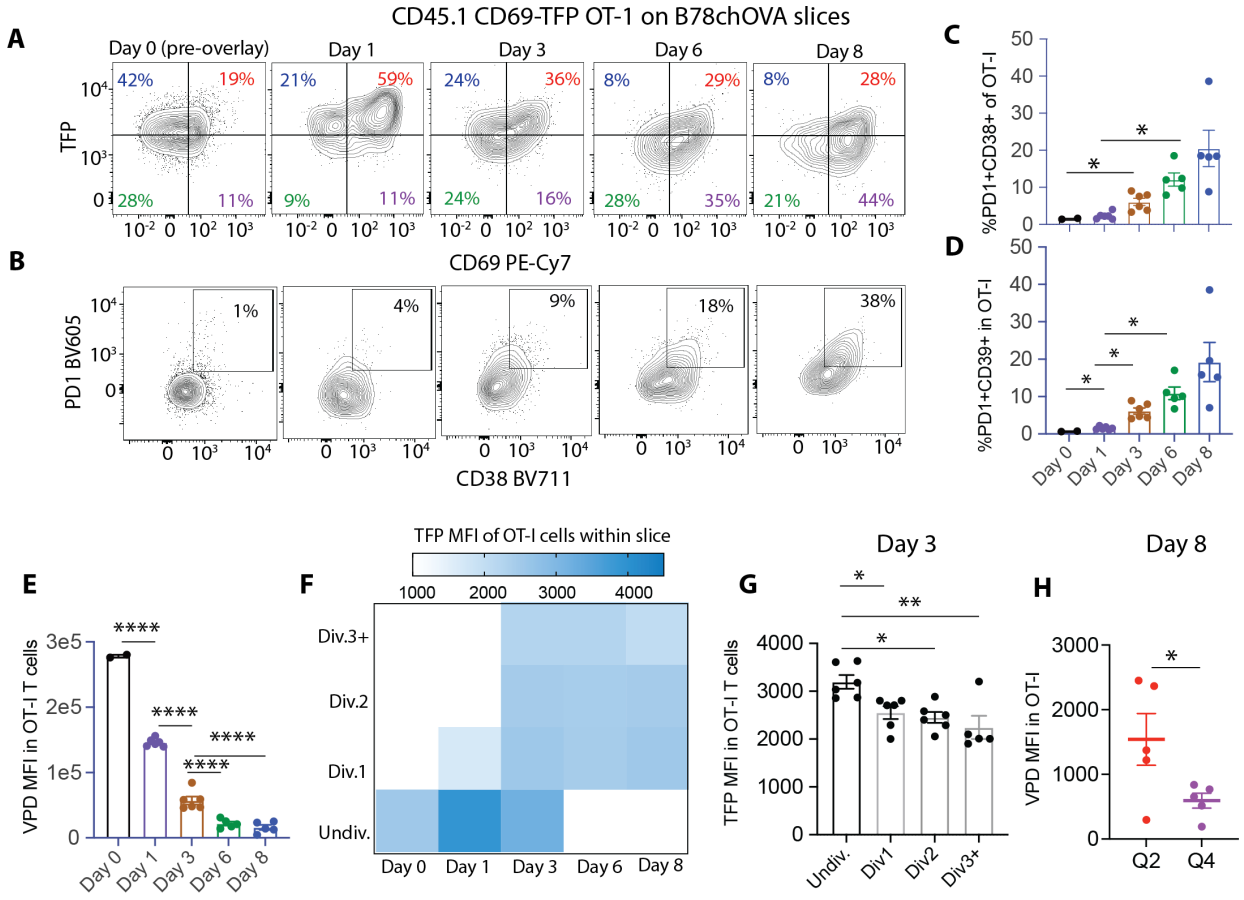

926

927 **Fig. S7: Ex vivo tumor slice overlay culture mimics CD69:TFP dynamics in vivo (A)**
928 Representative flow cytometry plots of **(E)** TFP vs. CD69 and **(F)** PD1 vs. CD38 expression in
929 slice-internal OT-I T cell from Day1-Day8, compared to Day0 (pre-overlay); **(B)** %PD1+CD38+,
930 **(C)** %PD1+CD39+ and **(E)** Violet proliferation dye (VPD) MFI of Day 0 pre-overlay and slice-
931 internal OT-I T cells at different time points after slice overlay (Day1-Day8); **(F)** heatmap of
932 average TFP MFI of OT-I CD8 T cells at Day 0 pre-overlay and derived from slice culture from
933 Day 1-Day 8 grouped by estimated number of divisions (>=3, 2, 1, or divided) and **(G)**
934 corresponding bar graph showing this quantification for Day 3; (H) VPD MFI of slice-internal OT-
935 Is from Q2 and Q4 at Day8; Bar graphs and line plots show mean +/- SEM, null hypothesis testing
936 by ANOVA and post hoc Holm-Šídák test, or paired t test in H; data are representative of 2
937 independent experiments, each 5-6 slices/time point for each slice experiment and Day 0 pre-
938 overlay samples in duplicate; TFP gated on WT controls CD8 T cells.

939

940

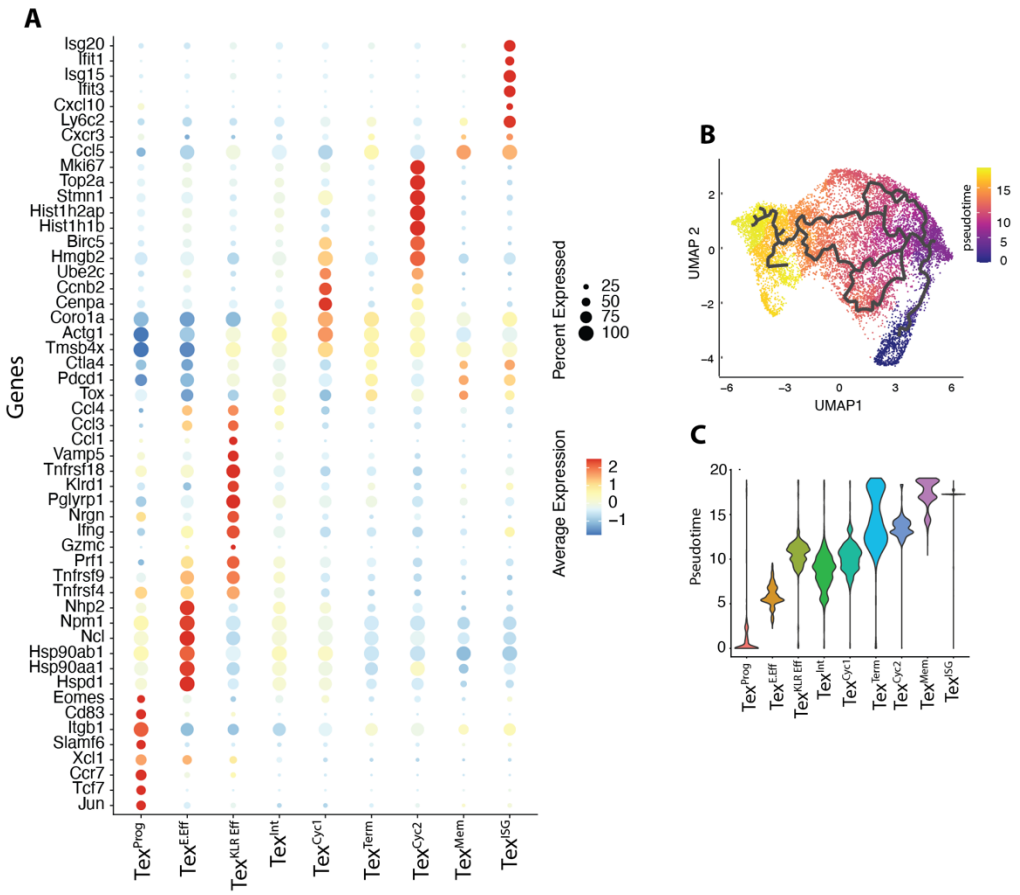

941

942 **Fig. S8: Gene expression based clustering of intratumoral OT-Is (A)** Dotplot representation
943 of differentially expressed and canonical T_{EX}-associated genes across the computationally
944 derived cell clusters from the scSeq of intratumoral Cd69-TFP:OT-I CD8 T cells at d12 post
945 injection into B78chOVA tumor-bearing mice; **(B)** UMAP representation of the scSeq data color-
946 coded by pseudotime derived from Monocle3 trajectory analysis; **(C)** Pseudotime spread of each
947 cluster.

948

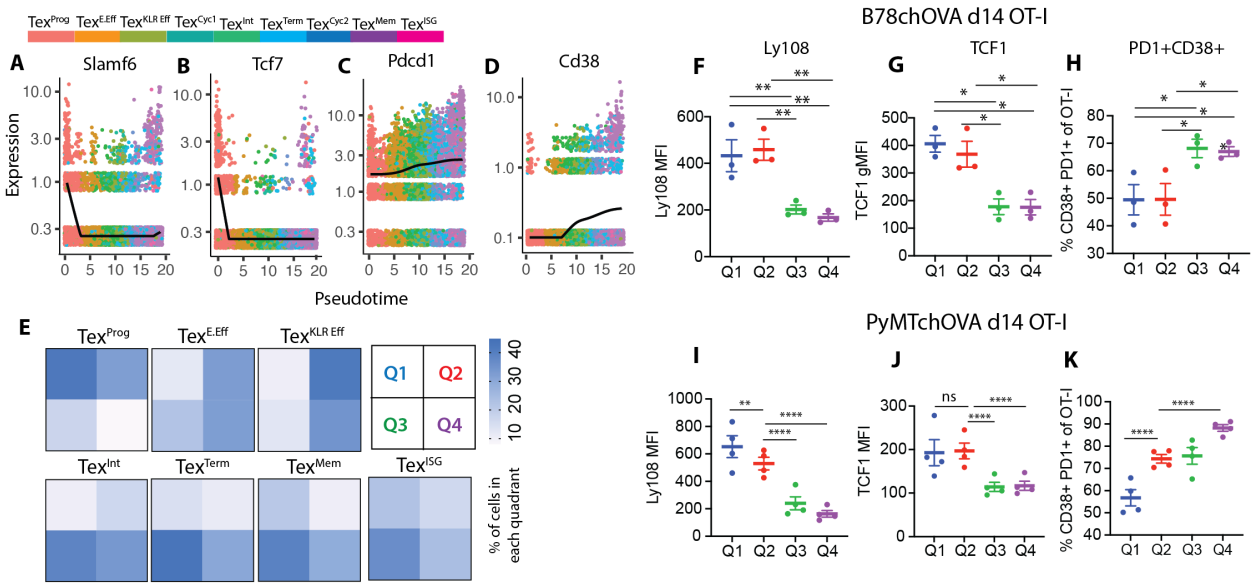

Fig. S9:Progenitor, intermediate and terminally exhausted CD8 T cells distribute distinctly among CD69:TFP quadrants (A-D) expression of select genes plotted against pseudotime and color-coded by clusters; best-fitting spline (degrees of freedom=5) to the gene expression pattern overlaid in black, random vertical jitter added to the plot for better visualization; **(E)** heatmaps of percentage of cells by CD69:TFP quadrants Q1-Q4; flow cytometric analysis of select markers from OT-I T cells isolated from **(F-H)** B78chOVA or **(I-K)** PyMTchOVA tumors 14 days post T cell injection grouped by quadrants; (data are mean +/- SEM, representative of >=2 independent experiments with 3-5 mice per experiment, null hypothesis testing by paired RM ANOVA with post-hoc paired t-tests).

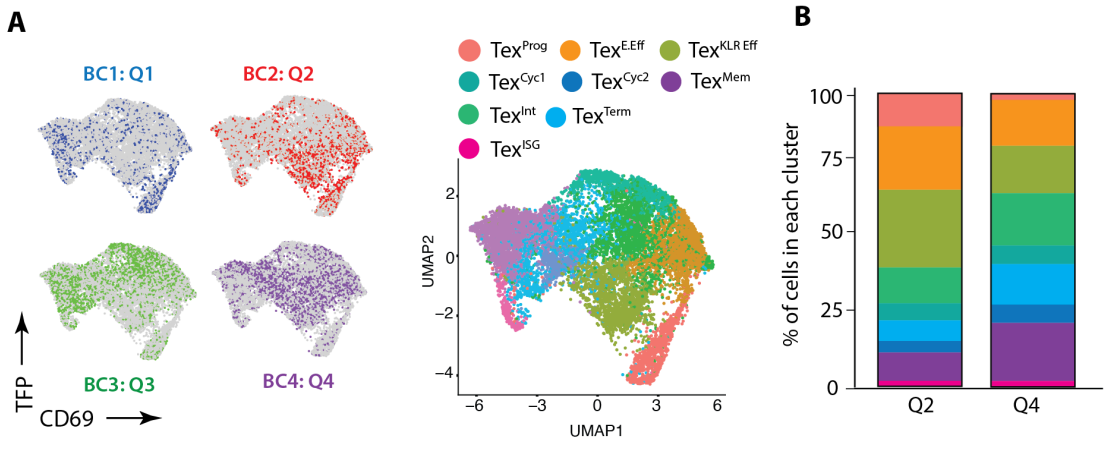

961 **Fig. S10:Q2 is enriched in effectors but not devoid of terminally differentiated T cells. (A)**
962 Overlay of each CD69:TFP quadrant in the UMAP space with the corresponding clusters shown
963 side-by-side; **(B)** Stacked bar plot showing the distribution of cells in the computationally-defined
964 clusters among all Q2 and Q4 cells.

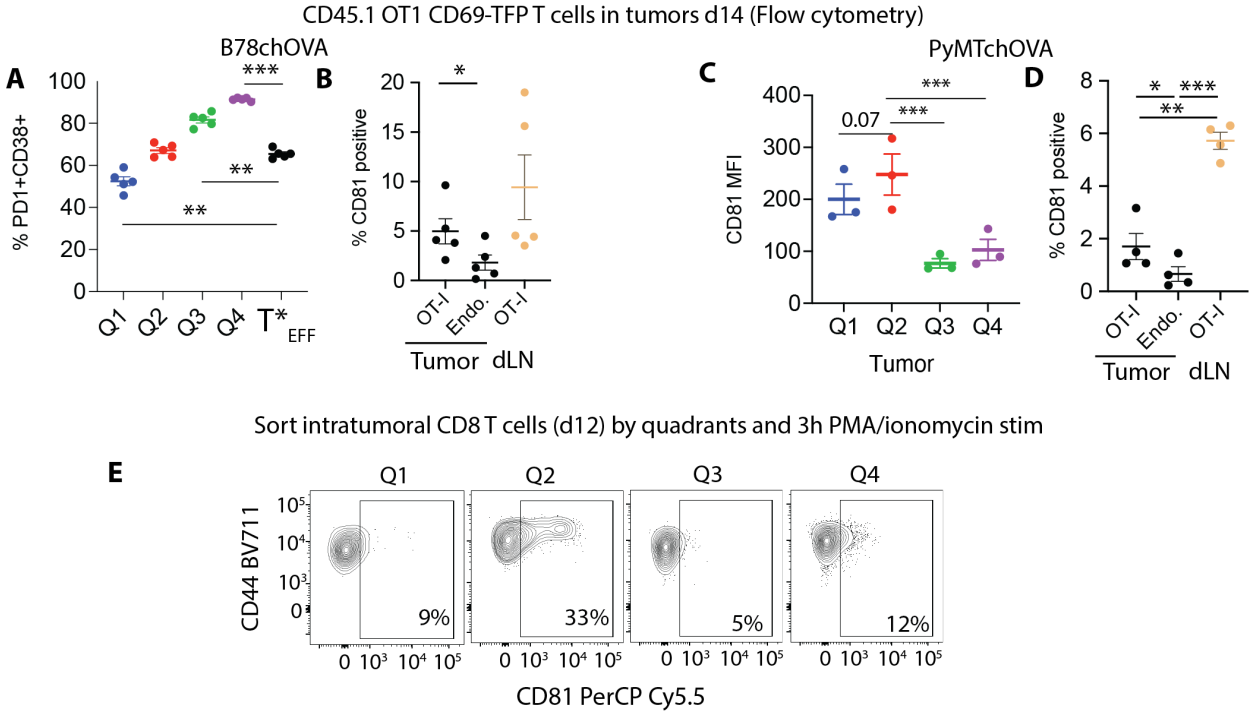

965

966 **Fig. S11: CD81 marks a rare subset of cells in Q2 (A)** %PD1+CD38+ of d14 intratumoral OT-I
967 T cells in B78chOVA tumors grouped by quadrants and with a subgating to show CD81+ Q2
968 (T^*_{EFF}) cells; **(B)** % CD81+ among d14 intratumoral OT-I, endogenous T cells and OT-I T cells in
969 the dLN of mice bearing B78chOVA tumors **(C)** CD81 expression in d14 intratumoral OT-I T cells
970 in PyMTchOVA tumors grouped by quadrants and **(D)** % CD81+ among d14 intratumoral OT-I,
971 endogenous T cells and OT-I T cells in the dLN of mice bearing PyMTchOVA tumors (data
972 representative of 2 independent experiments with 3-4 tumors per experiment; **(E)** CD81
973 expression among the quadrant-sorted populations; Bar graphs show mean +/- SEM; null
974 hypothesis testing by RM ANOVA and post hoc paired t test (A, C) and by ANOVA and post hoc
975 Holm-Šídák test (B, D).

976

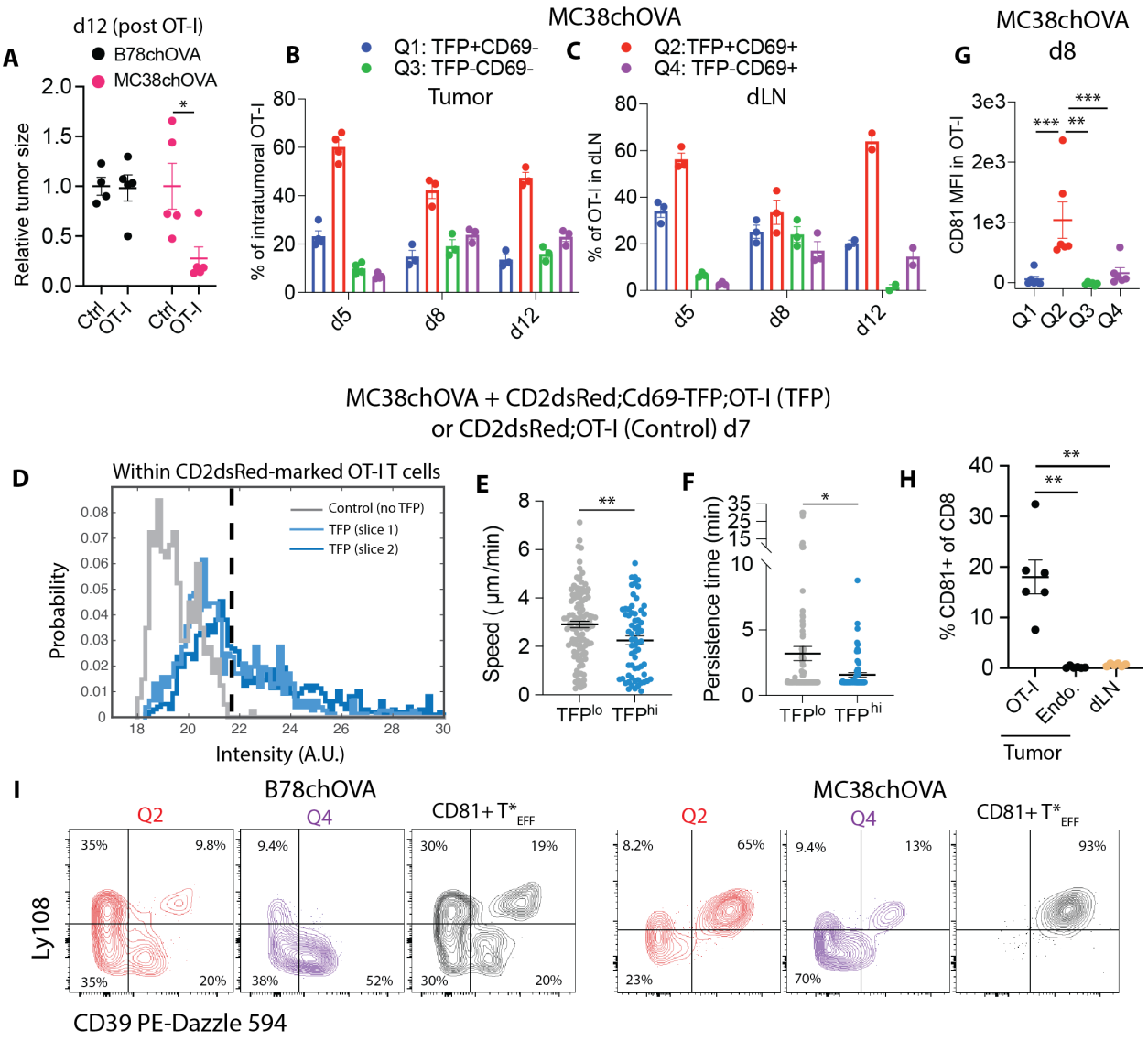

Fig. S12: **Features of Q2 OT-I T cells in MC38chOVA tumors. (A)** B78chOVA and MC38chOVA tumor sizes relative to the mean of the Ctrl group d12 post adoptive transfer of Cd69-TFP;CD45.1;OT-I T cells; in Bar graphs showing TFP:CD69 quadrant distribution among OT-I CD8 T cells in **(B)** tumors and **(C)** tdLN at d5, d8, d12 post T cell injection into MC38chOVA tumor-bearing mice corresponding dLNs (n=3-4 mice per group respectively); **(D)** Representative histograms of channel intensity within OT-I T cells in live tumor slices to find TFP^{hi} cells using CD2dsRed and CD2dsRed;Cd69-TFP OT-Is; **(E)** Speed and **(F)** Persistence of TFP^{hi} vs. TFP^{lo} intratumoral OT-Is d8 post adoptive transfer within live MC38chOVA tumor slices; **(G)** CD81 expression in d8 intratumoral OT-I T cells grouped by quadrants; **(H)** % CD81+ among d8 intratumoral OT-I, endogenous T cells and OT-I T cells in the dLN of mice bearing B78chOVA tumors; **(I)** Ly108 vs. CD39 expression profiles in d12 (B78chOVA) and d8 (MC38chOVA)

intratumoral OT-Is, separated by Q2, Q4 and CD81+ T*$_{EFF}$ subsets; bar graphs show mean +/- SEM, null hypothesis testing by unpaired t test (A), Mann-Whitney U test (E, F), paired RM ANOVA with post-hoc paired t-tests.

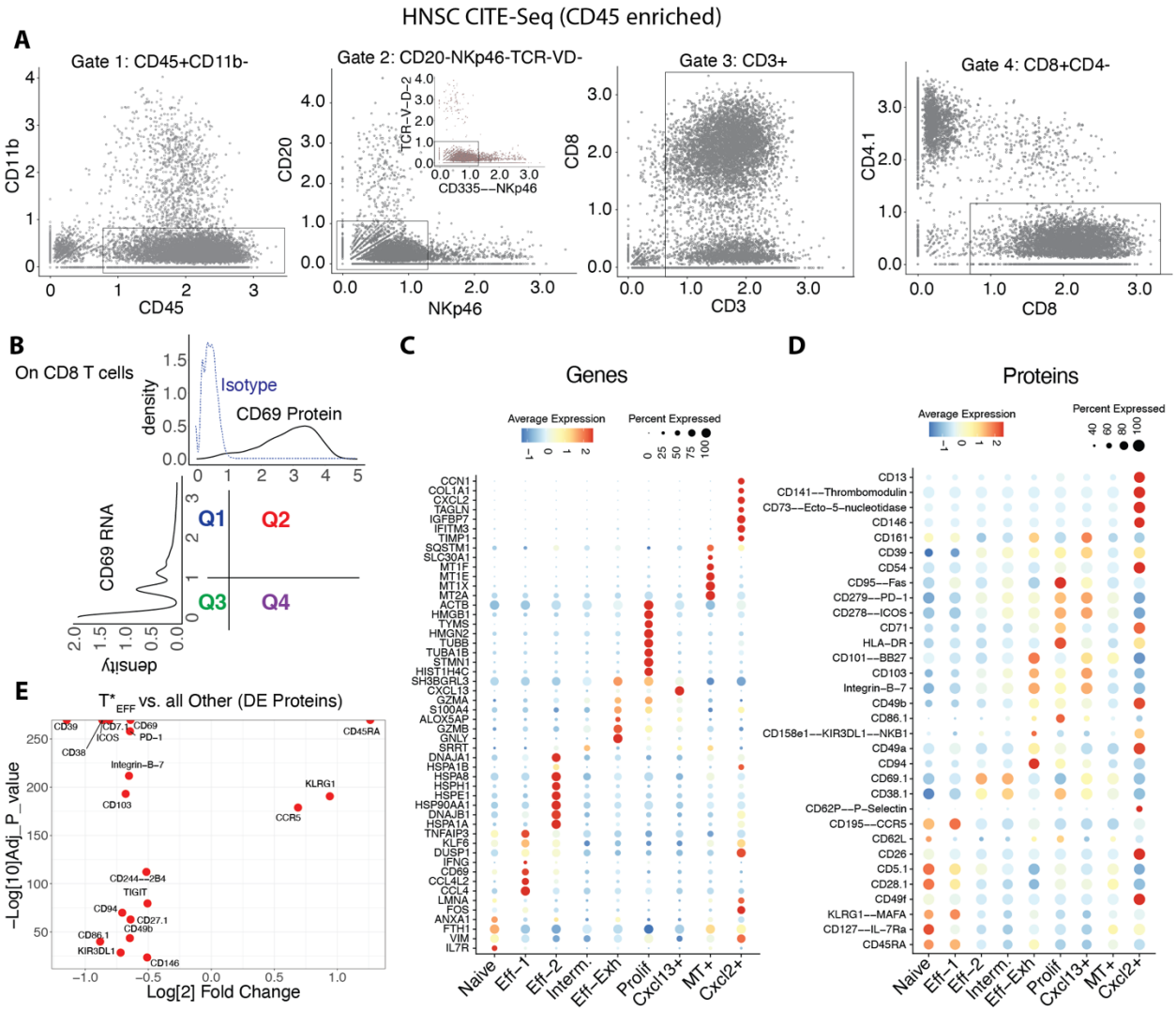

Fig. S13: **CITE-Seq of HNSC tumor sample allows mapping of quadrants onto cell phenotypes (A)** Gating scheme of CD45-enriched HNSC CITE-Seq data using protein markers to isolate a pure CD8 population; **(B)** Gating of the CD8 population into CD69 Protein: CD69 RNA quadrants; **(C)** DEGs and **(D)** DE Proteins for the computationally derived subsets obtained through multimodal clustering using both protein and RNA; **(E)** Volcano plot showing DE Proteins in the T*$_{EFF}$ (Q2 ∩ Eff-1) vs. all other CD8 T cells pre-filtered by a p-value <0.01 and average abs(log_2 fold change) >0.5;

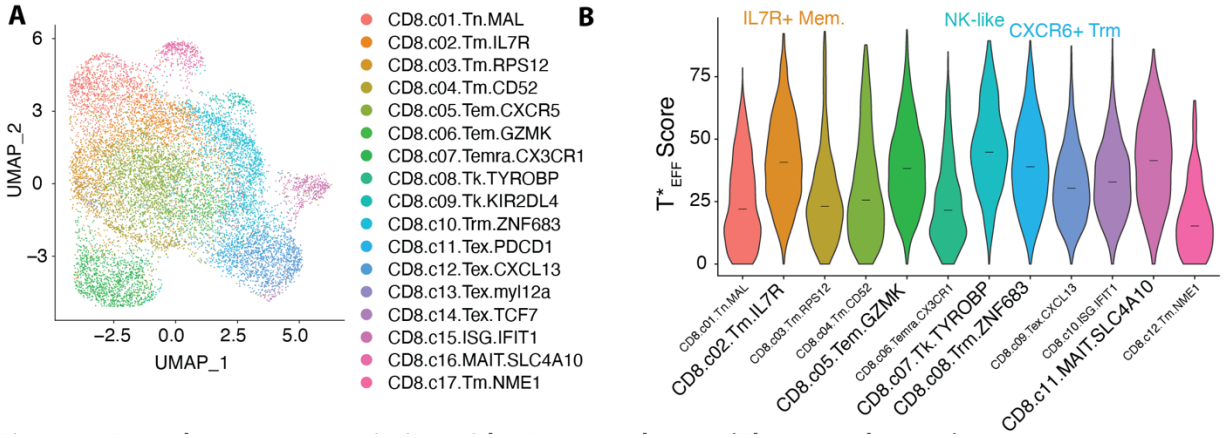

Fig. S14: **T*$_{EFF}$ phenotype association with CD8 metaclusters**. **(A)** UMAP representation of computationally-derived subsets among CD8 T cells in a pan-cancer T cell atlas(*30*) and **(B)** Violin plot showing the T*$_{EFF}$ signature score across those subsets – black line denotes median.